

New features in DPMJET version II.5

J. Ranft

Physics Dept. Universität Siegen, D-57068 Siegen, Germany, e-mail: Johannes.Ranft@cern.ch

(June 5, 2021)

DPMJET is a Monte Carlo model for sampling of hadron–hadron, hadron–nucleus, nucleus–nucleus and neutrino–nucleus interactions at accelerator and Cosmic Ray energies according to the two–component Dual Parton Model

Here we describe new features in version DPMJET–II.5: Implementation of new DPM diagrams for an improved description of baryon stopping in nuclear collisions and improvements in the calculation of Glauber cross sections. The new diagrams allow two quite different extrapolations of the model to the highest Cosmic Ray energies. The new version of the model is compared to experimental data on hadron–hadron, hadron–nucleus and nucleus–nucleus collisions.

Siegen preprint SI–99–5

I. INTRODUCTION

In the present paper we describe new features in the physics of DPMJET–II.5 and compare important features of the model to experimental data. The code manual for DPMJET–II.5 will be given in a separate paper [1].

The DPMJET–II.2 event generator was described in detail before [2–4]. The main topic in switching to DPMJET–II.3/II.4 [5] was the extension of the model up to energies of $\sqrt{s} = 2000$ TeV. The two versions DPMJET–II.3 and DPMJET–II.4 did differ mainly by the versions of the Lund code JETSET they use. DPMJET–II.3 did use a JETSET version transformed into DOUBLE PRECISION. DPMJET–II.4 uses the 1997 version PYTHIA–6.1 now in DOUBLE PRECISION in which JETSET is contained. DPMJET–II.5 continues to use PYTHIA–6.1. The extension to higher energies was done in DPMJET–II.3/4 by calculating the minijet component of the model using as default the GRV–LO94 parton distributions [6]. This is replaced in DPMJET–II.5 by the more recent version GRV–LO–98 [7]. These new parton distributions describe the data measured in the last years at the HERA Collider.

DPMJET–II is used in Collaboration with Battistoni, Carboni and Forti [8] for the simulation of the Cosmic Ray cascade in the HEMAS–DPM code system. A hadron production model to be used for simulations at accelerator and Cosmic Ray energies should use all possible information from fixed target experiments and collider experiments at accelerators. There might be large differences on what is considered important: Best studied at accelerators is the central region in hadron–hadron collisions. For studying the Cosmic Ray cascade, the main interest is in the forward fragmentation region of hadron–nucleus and nucleus–nucleus collisions. DPMJET simulates hadron production in the framework of the Dual Parton Model with emphasis as well in the central as in the fragmentation region.

Soft multiparticle production characterizing hadronic interactions at supercollider or Cosmic Ray energies cannot be understood purely within theoretical approaches provided by perturbative QCD. The nonperturbative soft component of hadron production, which is responsible for all of hadron production at low energies is still acting at higher energies together with the hard component described by perturbative QCD.

Using basic ideas of the dual topological unitarization scheme [9,10] the Dual Parton Model (DPM) [11] (a published review stressing mainly non-Monte Carlo applications is given in Ref. [12], a nice review, also with emphasis to Monte Carlo implementations of the DPM–model and to photon induced reactions can be found in the Ph.D Thesis of Ralph Engel [13]) has been very successfully describing soft hadronic processes together with the gradual transition to hard collisions with rising energy.

Observations like rapidity plateaus and average transverse momenta rising with energy, KNO scaling violation, transverse momentum–multiplicity correlations and *minijets* pointed out, that soft and hard processes are closely related. These properties were understood within the two–component Dual Parton Model [14–20].

The hard component is introduced applying lowest order of perturbative hard constituent scattering [21]. Single diffraction dissociation is represented by a triple–pomeron exchange (high mass single diffraction) and a low mass component.

The Dual Parton model provides a framework not only for the study of hadron–hadron interactions, but also for the description of particle production in hadron–nucleus and nucleus–nucleus collisions at high energies. Within this model the high energy projectile undergoes a multiple scattering as formulated in Glaubers approach; particle

production is realized by the fragmentation of colorless parton–parton chains constructed from the quark content of the interacting hadrons and nuclei.

The first successfull applications of the Monte Carlo version of the dual parton model (DPM) to hadron–nucleus [22,23] and nucleus–nucleus [24–26] collisions also demonstrated that the cascade of created secondaries in the target (and projectile) nuclei contributes significantly to particle production in the target (and projectile) fragmentation regions. DPMJET uses the concept of a formation zone [27,28] suppressing in a natural way the cascading of high–energy secondaries. The Monte Carlo model includes intranuclear cascade processes of the created secondaries combined with the formation time concept since the first version of DPMJET-II. The FZIC (formation zone intranuclear cascade) was also introduced for the projectile nucleus and in addition the nuclear evaporation and fragmentation of the residual nucleus was introduced into DPMJET-II [29,30].

In the following we briefly sketch new features of the model and mention the most important ingredients; for a more detailed description of the model as applied in the code we refer to Refs. [5,4,22,23,31–38,29,30,39–41]. The application of DPMJET to neutrino–nucleus interactions is described in [42]. In Section II we will describe new features of the Dual Parton Model as used in DPMJET-II.5. The most important of these new features are new diagrams contributing to baryon stopping and a better calculation of Glauber cross sections. In Section III we compare the model to data and in Section IV we discuss the properties of the model at the highest energies. In both these Sections we present only material obtained with DPMJET-II.5. It is not to be expected that in the energy region where experimental data are available the model has changed so strongly, that comparisons given in former papers with previous versions of the model would have become invalid.

What is new in DPMJET-II.5?

Here we only summarize the new features of DPMJET-II.5 against DPMJET-II.3/4 [5], which are described in more detail in later Sections.

Modifications of the Glauber model calculation of nuclear cross sections. For some light nuclei the Woods–Saxon nuclear densities are replaced by parametrizations in better agreement to data and measured nuclear radii are used [43] instead of the nuclear radii according to a parametrization used before. The new option XSECNUC is added to calculate a table of total, elastic, quasi–elastic and production cross sections using a modified version of the routine XSGLAU adopted from DTUNUC-II [44,45]. These changes lead to an improved agreement to measured nuclear cross sections, especially the p–Air cross sections measured in Cosmic Ray experiments.

Elimination of some old features of the code. Originally, DPMJET was written in single precision and compiler options were used on 32 bit word computers to transform the code to DOUBLE PRECISION. Now DPMJET is written explicitly in DOUBLE PRECISION. A number of features of the code was changed to get it running on different UNIX systems, especially HP–unix, DEC–alphas, IBM–unix, Sun–workstations and LINUX.

Old features of the code were removed, in particular: the optional fragmentation of strings according to the BAMJET code [46,47]. Only the PYTHIA (JETSET)string fragmentation remains in the present DPMJET, we use PYTHIA–6.1 in the DOUBLE PRECISION version. However, the internal particle codes used are still the ones from BAMJET, The output particle codes are as before the ones according to the PDG convention. Some of the older parton structure functions are dropped from the code. The chain fusion option, which was no longer up to date, has been removed.

Single diffraction also implemented in nucleus–nucleus collisions. The present version of the model DPMJET-II.5 allows to include or exclude single diffractive events also in the case of nucleus–nucleus collisions or to sample only single diffractive events. The diffractive cross section in hadron–nucleus and nucleus–nucleus collisions is calculated by the Monte Carlo method.

Implementation of new DPM diagrams for an improved description of baryon stopping in hadron–nucleus and nucleus–nucleus collisions. A new striking feature of hadron production in nuclear collisions is the large stopping of the participating nucleons (compared to hadron–hadron collisions) in hadron–nucleus and nucleus–nucleus collisions [48,49]. The popcorn mechanism implemented in models with independent string fragmentation like the DPM since more than 15 years is not sufficient to explain this enhanced baryon stopping. New DPM–diagrams were proposed by Capella and Kopeliovich [50] and investigated in detail by Capella and Collaborators [51,52] and by Casado [53]. DPMJET-II.5 implements these diagrams and obtains an improved agreement to net–baryon distributions in nuclear collisions.

Implementation of the new diagrams allows for two different extrapolations of the model to Cosmic Ray energies beyond the accelerator energy range. The diagram investigated by Capella and Collaborators [51,52] uses sea quarks, which in nuclear collisions according to the Glauber model are needed to implement the multiple collisions in the nucleus. In the Dual Parton Model in the collider energy range there are further multiple collisions, again implemented using sea quarks at the ends of multiple chains, which occur due to the unitarization procedure.

We get at high energy enhanced baryon stopping even in proton–proton collisions and a strong modification of the model if also these sea quarks are used in the new diagrams. The two models obtained with or without this effect

result in quite different model predictions at the highest Cosmic Ray energies.

Improvements in the sampling and analysis of central collisions. Older versions of DPMJET were also applied to central heavy ion collisions at CERN-SPS, RHIC and LHC energies. The previous version of DPMJET DPMJET-II.3/4 [5], was mainly implemented with the aim to sample minimum bias hadron–nucleus and nucleus–nucleus collisions for the simulation of the Cosmic Ray cascade. Heavy targets or projectiles like Pb or Au and central collisions are rather unimportant for this purpose.

Many new, previously unknown features of multiparticle production have been found by the experimental heavy ion program at the CERN-SPS. It is certainly useful to use these results as a check even if the aim would be just to simulate Cosmic Ray events. Important features of these results concern in particular strangeness production and the baryon stopping discussed already above in central nucleus–nucleus collisions.

DPMJET-II.5 does not describe all features of the heavy ion experiments, nevertheless, it has been tuned to work for central collisions and to describe already quite a number of features of the CERN-SPS heavy ion data.

II. BASIC PHYSICAL CONCEPTS OF THE DUAL PARTON MODEL

A. The two-component Dual Parton Model for hadron–hadron collisions

The two component Dual Parton model for hadron–hadron collisions as applied in DPMJET has been described in detail in [5,2,15,20]. We will not repeat this here.

The only topic which has to be discussed is the fit of the model parameters using the new parton structure function GRV-LO-98 [7].

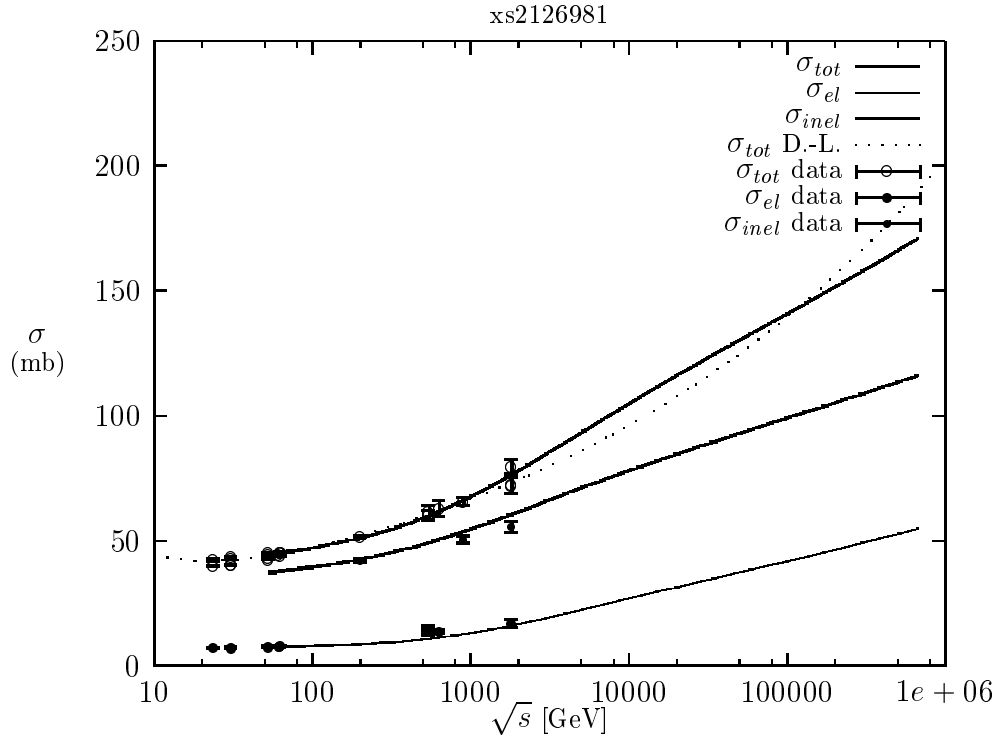


FIG. 1. Total, inelastic and elastic $p\bar{p}$ and pp cross sections as function of the center of mass energy \sqrt{s} . The model results obtained using the GRV-LO98 parton distributions [7] are compared to the Donnachie–Landshoff fit for the total cross section [54] and to data [55–63].

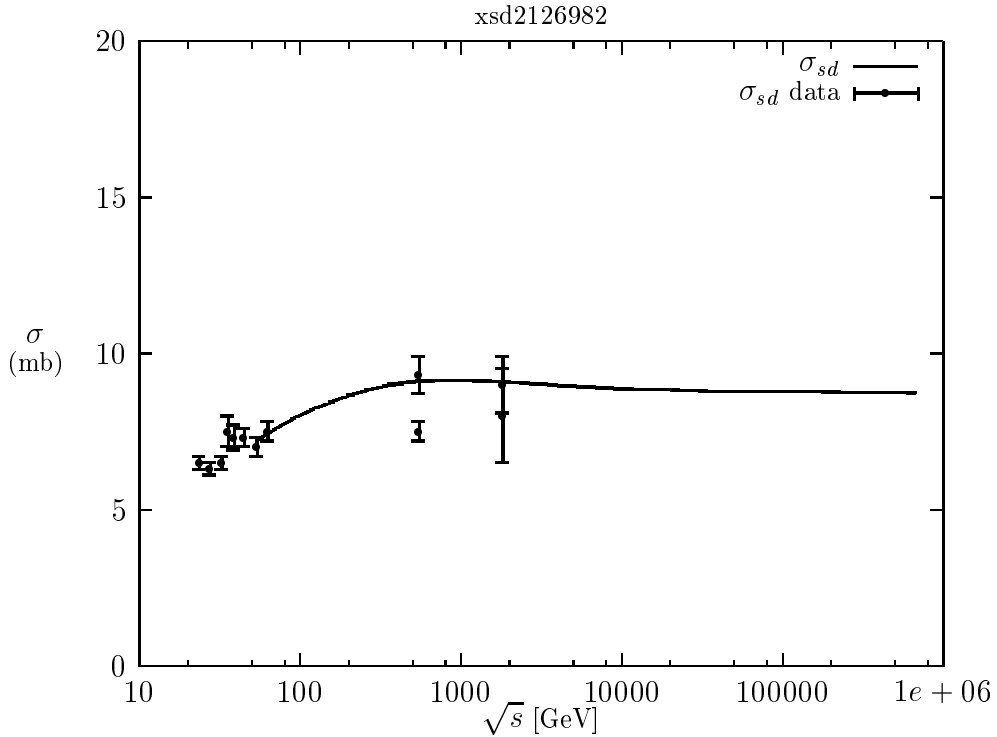


FIG. 2. Single diffractive $p\bar{p}$ and pp cross sections as function of the center of mass energy \sqrt{s} . The model results obtained using the GRV-LO98 parton distributions [7] are compared to data for $M^2/s = \xi \leq 0.05$ [64–68]. to data.

We fit the Pomeron parameters with the energy dependent p_\perp cut-off [20] for minijets:

$$p_{\perp thr} = 2.5 + 0.12[\log_{10}(\sqrt{s}/\sqrt{s}_0)]^3 \quad [\text{GeV}/c], \quad \sqrt{s}_0 = 50 \text{ GeV}. \quad (2.1)$$

To describe the high energy particle production we have to determine the free parameters of the model, i.e. the proton-Pomeron coupling constant g , the effective soft Pomeron intercept $\alpha(0)$, the slope of the Pomeron trajectory α' , the slope parameters b and b_h and the excitation coupling constant λ . This has been done by a global fit to all available data of total, elastic, inelastic, and single diffractive cross sections in the energy range from ISR to collider experiments as well as to the data on the elastic slopes in this energy range. Since there are some differences in the hard parton distribution functions at small x values resulting in different hard input cross sections we have to perform separate fits for each set of parton distribution functions.

We get good fits using the GRV-LO-98 PDF. In Table I we give the parameters obtained in the fit. The values obtained for $\alpha(0)$ demonstrate again that the fits result in a supercritical Pomeron. In Fig. 1 we plot the fitted cross sections together with the data. Furthermore we compare the total cross sections obtained with the popular Donnachie-Landshoff fit [54]. In Fig. 2 we plot the fitted single diffractive cross sections together with data [64–68].

TABLE I. DTUJET99 model parameters obtained with an energy dependent $p_{\perp thr}$.

PDF set	$g^2(\text{mb})$	$\alpha(0)$	$\alpha' [\text{GeV}^{-2}]$	$b [\text{GeV}^{-2}]$	$b_h [\text{GeV}^{-2}]$	λ
GRV-LO-98	55.16	1.0513	0.325	1.114	1.70	0.585

The single diffractive cross section becomes energy independent at high energies in DTUJET and DPMJET. This follows from the triple Pomeron cross section chosen in [15] without the energy rise according to the supercritical Pomeron. (As explained in detail elsewhere DPMJET follows in the unitarization procedure DTUJET.) Such an approximation is not necessary in the Dual Parton Model. It has been shown by Engel within the PHOJET Dual Parton Model [69] that the proper inclusion of the supercritical triple Pomeron cross section as well as higher order terms like the double pomeron graph into the unitarization procedure also results in a single diffractive cross section becoming rather energy independent at high energy in agreement to the data. Similar results were obtained by Gotsman, Levin and Maor [70]. On a phenomenological basis this saturation of the single diffractive cross section was described by Goulianos [71] using the term of a *renormalized flux*.

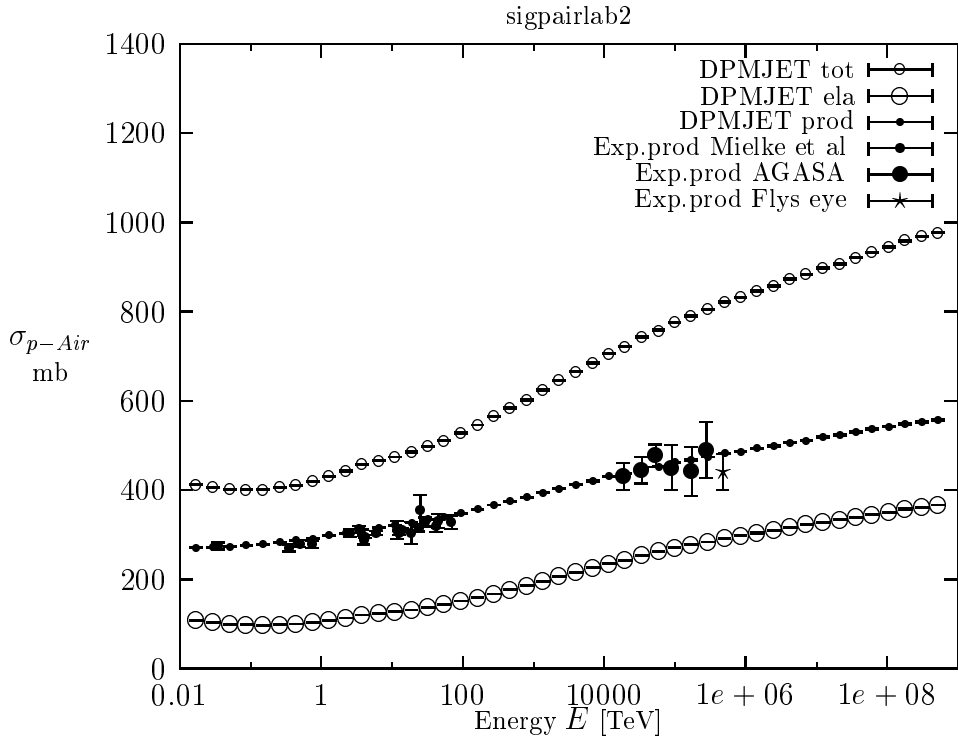


FIG. 3. The inelastic (production) cross section σ_{p-Air} calculated by DPMJET-II.5 as function of the laboratory collision energy (from 0.01 TeV up to 10^9 TeV) compared to experimental data collected by Mielke et al. [72] and to experimental data from the AGASA [73] and Fly's eye [74] experiments as presented in corrected form in a recent paper by Block, Halzen and Stanev [75]. Given are also the calculated total and elastic cross sections.

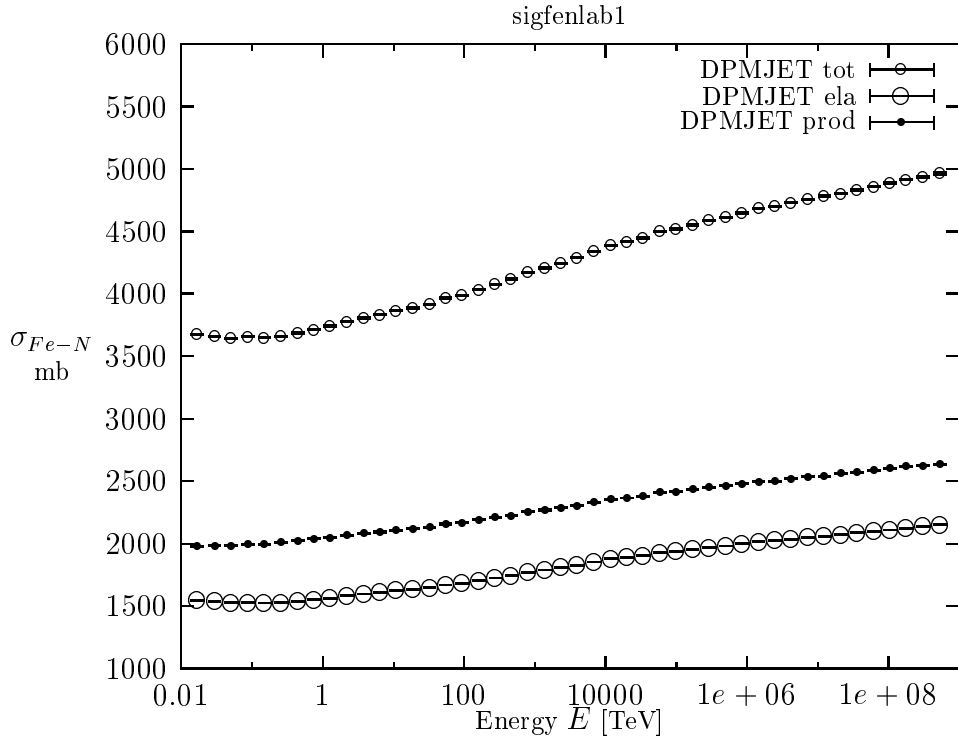


FIG. 4. The inelastic (production) cross section σ_{Fe-N} calculated by DPMJET-II.5 as function of the laboratory collision energy (from 0.01 TeV up to 1.E9 TeV). Given are also the calculated total and elastic cross sections.

B. The Dual Parton Model for hadron production in hadron–nucleus and nucleus–nucleus collisions

In the following we discuss new features in DPMJET-II.5, for a more detailed description of the model as applied in the code we refer to Refs. [22,23,31,32,34,35,37,76,29,30,41].

1. The Monte Carlo realization of the dual parton model DPMJET for hadron-nucleus and nucleus-nucleus collisions

The model starts from the impulse approximation for the interacting nuclei – i.e. with a frozen discrete spatial distribution of nucleons sampled from standard density distributions [77,43]. The primary interaction of the incident high-energy projectile proceeds via n elementary collisions between $n_p = n_A$ and $n_t = n_B$ nucleons from the projectile (for incident hadrons $n_p = 1$) and the target nuclei, resp., . Actual numbers n, n_p and n_t are sampled on the basis of Glauber’s multiple scattering formalism using the Monte Carlo algorithm of Ref. [77].

The Glauber model, which is part of DPMJET-II allows to calculate the inelastic hadron–nucleus cross sections. The needed ingredients of this calculation are the nuclear geometry and the elementary hadron–nucleon scattering amplitude.

The nuclear matter distribution is parametrized as follows:

For most nuclei (untill DPMJET-II.3/4 all nuclei) we parametrize the average nuclear radius (in fm)

$$c = \sqrt{r^2} = 1.12 N_a^{0.33} \quad (2.2)$$

This parametrization is however not reliable for some light nuclei important for Cosmic Ray collisions. Therefore we replace (2.2) for these nuclei by the values given in Table 2 [43].

Table 2. Average nuclear radii used in DPMJET-II.5 [43] (in fm).

N_a	9	10	11	12	13	14	15	16	17	18
$\sqrt{r^2}$	2.52	2.45	2.37	2.45	2.44	2.55	2.58	2.71	2.66	2.72

The nuclear density distribution is parametrized for most nuclei as the Fermi distribution

$$F(r) = \frac{1}{1 + \exp \frac{r-c}{0.545}} \quad (2.3)$$

However, for N_a between 9 and 18 we use again more precise density distributions as given in Ref. [43].

The elementary hadron–nucleus scattering amplitude is parametrized as follows:

Energy dependent quantities enter the Glauber approach via the profile function of elastic hadron-nucleon scattering,

$$\gamma_{hN}(b) = \frac{1}{2\pi i p} \int d^2 q \exp(i\vec{q} \cdot \vec{b}) f_{hN}(\vec{q}), \quad (2.4)$$

i.e. the amplitude of elastic hadron-nucleon scattering in the impact parameter representation (with \vec{q} denoting the lateral, i.e. two-dimensional momentum transfer). In their Monte Carlo realization of Glauber's approach Shmakov et al. [77] apply the high-energy approximation of the profile function,

$$\gamma_{hN}(b) = \frac{\sigma_{hN}^{tot}}{4\pi a} \left(1 - i \frac{\Re f_{hN}(0)}{\Im f_{hN}(0)} \right) e^{-\frac{b^2}{2a}}, \quad (2.5)$$

with parameters σ^{tot} , a and $\rho = \Re f_{hN}(0) / \Im f_{hN}(0)$ appropriate for the description of nucleus-nucleus interactions at energies of several GeV per nucleon. (This parametrization corresponds to a differential cross section $d\sigma/dt \simeq \sigma_{tot} \exp(a \cdot t)$ with $t \simeq -\vec{q}^2$.)

However, the energy dependence of the elastic hadron-nucleon scattering amplitudes will influence the properties of hadron–nucleus and nucleus–nucleus scattering. In particular, the number of individual high-energy hadron-nucleon interactions (n, n_A, n_B) will increase with rising energy, hence the multiplicity will increase stronger than to be expected from the energy dependence of single hadron-hadron interactions.

Guided by the data collected in Ref. [78], we apply the following parametrizations for the slope parameter a : $a = 8.5 (1 + 0.065 \ln s)$ for nucleon-nucleon collisions above $s = 50$ GeV 2 , $a = 6.2 (1 + 0.13 \ln s)$ for nucleon-nucleon collisions below $s = 50$ GeV 2 and $a = 6.0 (1 + 0.065 \ln s)$ for π - and K-nucleon collisions. We use for the ratio ρ of the real and imaginary part of the elastic scattering amplitude: $\rho = -0.63 + 0.175 \ln \sqrt{s}$ for the energy region $3.0 \leq \sqrt{s} \leq 50$. and $\rho = 0.1$ in the energy region $\sqrt{s} \geq 50$ GeV in nucleon-nucleon scattering and $\rho = 0.01$ for π - and K-nucleon scattering.

The energy dependence of the total cross sections is described by the fits of the Particle Data Group [79]; at energies beyond the range of the actual parametrization of the pp cross section the one for $\bar{p}p$ is applied and at energies even higher we use the total cross-sections as calculated by the two-component Dual Parton Model for hadron–hadron collisions, see also Fig.1.

The same information is also needed to construct the inelastic events and indeed for nuclear collisions each run of DPMJET starts with a calculation of the inelastic cross section.

A new option (XSECNUC) has been added to DPMJET-II.5 to calculate a table of hadron–nucleus or nucleus–nucleus cross sections as function of the collision energy. The routine XSGLAU (this is a routine adopted from DTUNUC-II [44,45]) using the method according to [77]) calculates the following cross sections:

$$(1) \sigma_{tot}^{A-B}$$

$$(2) \sigma_{el}^{A-B} \quad A + B \rightarrow A + B$$

$$(3) \sigma_{quasi-el-3}^{A-B} \quad A + B \rightarrow A + X, \text{ excluding (2)}$$

$$(4) \sigma_{quasi-el-4}^{A-B} \quad A + B \rightarrow X + B, \text{ excluding (2)}$$

$$(5) \sigma_{quasi-el-5}^{A-B} \quad A + B \rightarrow X, \text{ excluding (2),(3) and (4)}$$

$$(6) \sigma_{prod}^{A-B} = \sigma_{inel}^{A-B} = \sigma_{tot}^{A-B} - \sigma_{el}^{A-B} - \sigma_{quasi-el-3}^{A-B} - \sigma_{quasi-el-4}^{A-B} - \sigma_{quasi-el-5}^{A-B}$$

In Fig.3 and 4 we present the cross sections (only σ_{tot}^{A-B} , σ_{el}^{A-B} and σ_{prod}^{A-B}) as calculated by DPMJET-II.5 using the XSECNUC option for p–Air and Fe–N which are relevant for calculating the Cosmic Ray cascade as function of

the lab energy from 0.02 TeV to 10^9 TeV. The quasi-elastic cross sections $\sigma_{\text{quasi-}el-i}^{A-B}$ are only contained in these plots only in $\sigma_{\text{tot}}^{A-B}$. The inelastic DPMJET p–Air cross sections $\sigma_{\text{inel}}^{A-B}$ are compared to the experimental data collected by Mielke et al. [72] and to experimental data from the AGASA [73] and Fly’s eye [74] experiments as presented in corrected form in a recent paper by Block, Halzen and Stanev [75].

C. Implementation of new DPM diagrams for an improved description of baryon stopping in hadron–nucleus and nucleus–nucleus collisions

1. Diquark fragmentation, the popcorn mechanism

The fragmentation of diquarks is slightly more complicated than the fragmentation of a quark jet. As justified by Rossi and Veneziano [80] the baryon can be pictured as made out of three quarks bound together by three strings which join in a so called string junction point. In diagrams we can characterize the baryons

- (i) by the three quarks and the string junction or
- (ii) by a quark and a diquark, in this case the string junction always goes with the diquark.

In all the diagrams discussed in this section we will either plot the quark and the diquark or, if the diquark breaks, the three quarks and the string junction. The quarks and the two quarks of a diquark are plotted as solid lines, the string junction is plotted as a dashed line.

There are two possibilities for the first fragmentation step of a diquark, see Fig.5. Either we get in the first step a baryon, which contains both quarks of the diquark and the string junction or we get in the first step a meson containing only one of the two quarks and the baryon is produced in one of the following fragmentation step. This mechanism is well known, it is presented in the review on the Dual Parton Model [12] and it was investigated for instance in [81,82]. This mechanism was implemented from the beginning in the BAMJET–fragmentation code [47,46] used previously in DPMJET. This mechanism is also implemented under the name *popcorn* fragmentation in the Lund chain fragmentation model JETSET [83,84].

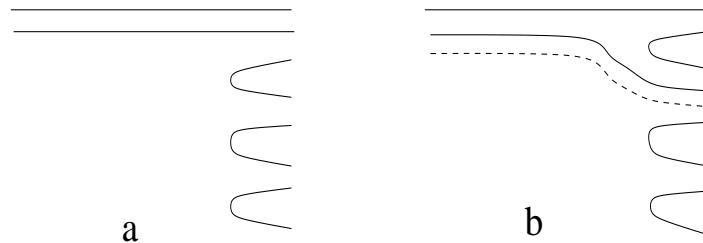


FIG. 5. (a) Conventional diquark fragmentation, the baryon is produced in the first fragmentation step. (b) The popcorn mechanism: a meson is produced in the first fragmentation step, the baryon appears in the second or later fragmentation steps. We plot the lines for the two quarks of the diquark as solid lines, the string junction is plotted as a dashed line.

What happens in the model with the popcorn mechanism compared to the model without can be most easily seen looking at the proton rapidity distribution in p–p collisions. The two maxima in the target and projectile fragmentation region of the proton rapidity distribution shift by about half a unity to the center, these maxima become wider and correspondingly the dip in the center is reduced. At the same time the Feynman x distributions of mesons get a component at larger Feynman x . The effects in hadron–nucleus and nucleus–nucleus collisions are quite similar. The popcorn mechanism is however not enough to explain the baryon stopping observed experimentally in hadron–nucleus and nucleus–nucleus collisions [48,49], this will be discussed in more detail in Section III.

2. New diquark breaking DPM diagrams in hadron–nucleus and nucleus–nucleus collisions

New diquark breaking DPM–diagrams mainly of interest in hadron–nucleus and nucleus–nucleus collisions were proposed by Capella and Kopeliovich [50] and investigated in detail by Capella and Collaborators [51,52,85]. Similar ideas were discussed by Vance and Gyulassy [86]. Capella and Kopeliovich [50] did discuss in detail their first diquark

breaking mechanism (see Fig.6, where this mechanism is characterized for nucleon–nucleon collisions), in this case the valence–diquark breaks into the two quarks, the baryon is produced in the second or in later fragmentation steps.

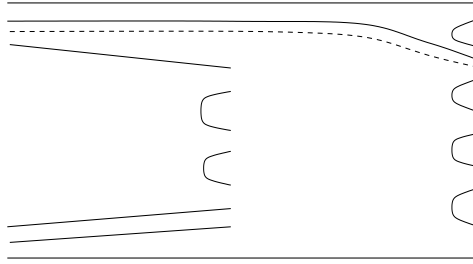


FIG. 6. The first C–K diquark breaking mechanism [50] plotted for a nucleon–nucleon collision.

Looking only at the diagrams, one does not see any difference between the popcorn mechanism and the first Capella–Kopeliovich (C–K) diquark breaking mechanism. However, the mechanism of this first (C–K) diquark breaking mechanism differ in detail from the popcorn mechanism discussed above. Nevertheless, implementing the first C–K mechanism in DPMJET did not give any new feature of baryon stopping, which could not also be obtained from the popcorn mechanism. Therefore, we continue to use in DPMJET-II.5 the popcorn mechanism instead of the C–K mechanism, there is no need to use both effects.

More interesting is the second C–K mechanism, which was proposed but not discussed in detail in [50]. This mechanism was discussed in detail by Capella and Collaborators [51,52,85]. In Fig.7 we plot first the diquark–conserving diagram for a nucleon–nucleus collisions with two participants of the target nucleus. This is the traditional way for such a collision in the DPM.

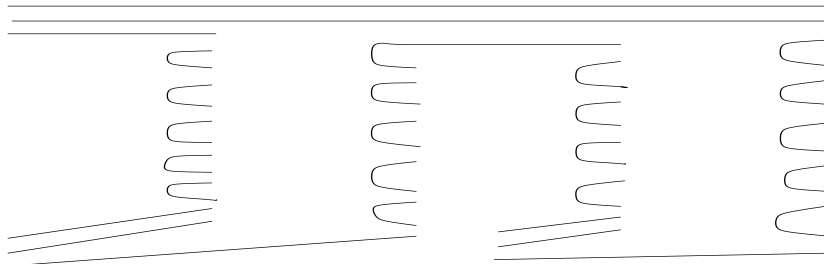


FIG. 7. The diquark–conserving diagram for a nucleon–nucleus collision with two participants of the target nucleus.

In Fig.8 we plot the second C–K diquark–breaking diagram for the same collision. Now the second valence quark from the broken diquark in the first C–K diagram in Fig.6 is replaced by a Glauber sea quark from the nucleon projectile. Therefore, we will call the mechanism the Glauber sea quark mechanism of baryon stopping GSQBS. The probability of such a diquark splitting rises if the considered nucleon is involved in more than two interactions. The GSQBS has been implemented in DPMJET-II.5 and we will see in Section III, that in nucleon–nucleus collisions and nucleus–nucleus collisions we are able with this mechanism to fill the dip in the baryon rapidity distributions at central rapidity in agreement to the experimental data. As discussed already in detail in [52,85] this mechanism also contributes to increase the Hyperon production in nucleon–nucleus and nucleus–nucleus collisions.

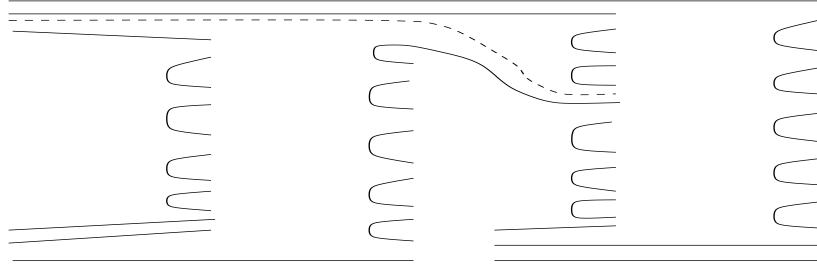


FIG. 8. The Glauber sea quark mechanism of baryon stopping GSQBS for a nucleon–nucleus collision with two participants of the target nucleus. This is the second C–K diquark–breaking mechanism [50].

3. The Casado diagram

A new diagram was also introduced by Casado [53]. The diagram is plotted again for a nucleon–nucleus collision with two participants of the target nucleus in Fig. 9. Here the fragmenting diquark contains a Glauber sea quark and hadronizes like a valence diquark producing baryons mainly in the fragmentation region. However, the flavor content of the baryon is changed. This diagram gives another contribution to hyperon production in nuclear collisions. We have implemented the Casado diagram in DPMJET-II.5 and it is used in addition to the GSQBS diagram for all nuclear collisions compared in Section III to data.

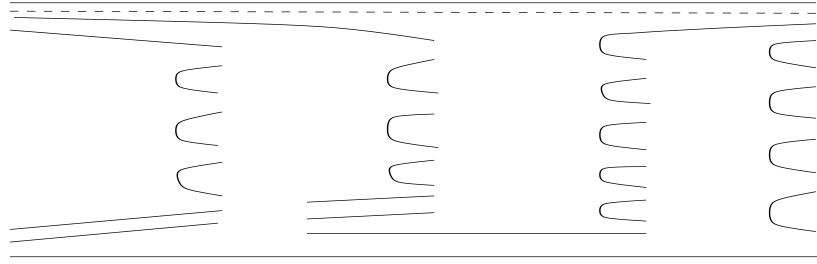


FIG. 9. The diagram introduced by Casado [53] for a nucleon–nucleus collision with two participants of the target nucleus. The diquark contains one Glauber sea quark.

4. Two extrapolations of DPMJET-II.5 to Cosmic Ray energies.

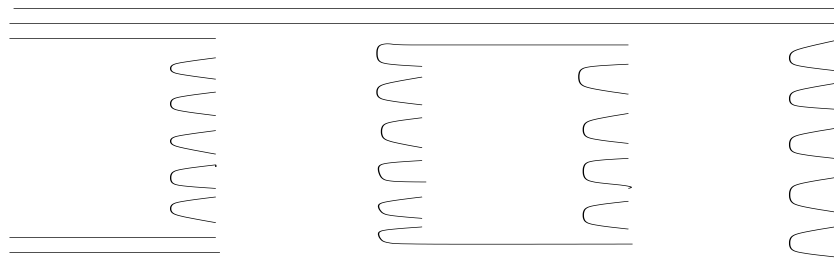


FIG. 10. Standard DPM diagram for a nucleon–nucleon interaction with one additional soft secondary interaction induced by the unitarization procedure. There is one valence–valence and one sea–sea interaction, each represented by a pair of chains.

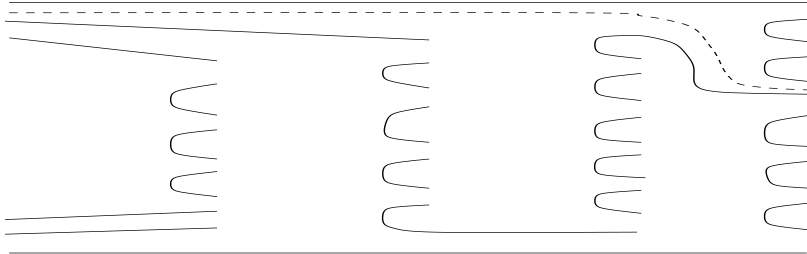


FIG. 11. New DPM diagram for a nucleon–nucleon interaction with one additional soft secondary interaction induced by the unitarization procedure. The diquark is split and an unitarity sea quark is used similar to Fig. 8 to shift the baryon in one of the chains. We call this the unitary sea quark mechanism for baryon stopping USQBS.

At high energies we have multiple collisions even in hadron–hadron collisions due to the unitarization procedure. We call the sea quarks at the ends of the additional chains in this case *unitary sea quarks*. The Glauber sea quarks are needed in nuclear collisions already at rather low energies, for instance at the energies of heavy ion collisions at the CERN–SPS. In contrast to this, unitary sea quarks appear in significant numbers in hadron–hadron and nuclear collisions only at rather high energies, for instance at the energies of the CERN–SPS collider or the TEVATRON collider, they are important in the Cosmic Ray energy region.

With the unitary sea quarks at the ends of the chains from the secondary collisions we obtain a new mechanism for baryon stopping, which will become effective at very high energies.

In Fig.10 we plot the standard DPM diagram for a nucleon–nucleon interaction with two soft interactions induced by the unitarization procedure. There is one valence–valence and one sea–sea interaction, each represented by a pair of chains. In analogy to Fig. 8 we construct from this the new diagram for baryon stopping in Fig. 11. The diquark is split and an unitary sea quark is used to have the baryon only in the second or later fragmentation steps in one of the chains. We call this the unitary sea quark mechanism for baryon stopping USQBS. Also here the probability for such a diquark splitting rises if there are more than 2 interactions of the hadrons involved. Obviously, this mechanism leads to Feynman x distributions of baryons in p–p collisions becoming softer and Feynman x distributions of mesons becoming harder than without the USQBS mechanism.

In contrast to the GSQBS mechanism, which leads already to effects in nuclear collisions at the energy of the CERN–SPS, we have at present no data available to prove that this USQBS mechanism is a valid extension of the DPM. There is no data for baryon stopping in proton–proton or antiproton–proton collisions at collider energies. Unfortunately, the fragmentation region at large Feynman x has not been investigated experimentally with enough detail at any of the hadron–hadron colliders. However, if the GSQBS mechanism is the correct mechanism responsible for the baryon stopping effects found in nuclear collisions, then also the USQBS mechanism should modify the collisions at collider energies and beyond. In Section IV, where we present the properties of DPMJET-II.5 at Cosmic Ray energies we present always two extrapolations of the model. In one version (shortly characterized as version 55 in the plots) we have both the GSQBS and USQBS mechanism, in a second version (characterized in the plots as version 50) we have only the GSQBS mechanism. Only collider experiments on baryon stopping or Cosmic Ray observations can prove, which version is the better one. From theoretical prejudices however there would be the claim, that the version with both the GSQBS and USQBS mechanisms is to be preferred.

5. New parameters connected with the diquark breaking diagrams

For each of the new diquark breaking diagrams described in this Section we have to introduce a new parameter. These parameters give the probability for the diquark breaking mechanisms to occur, given a suitable sea quark is available and given that the diquark breaking mechanism is kinematically allowed. For an original diquark–quark chain of small invariant mass, which originally just fragments into two hadrons, the diquark breaking is often not allowed at small energies.

The optimum values of the new parameters are determined by comparing DPMJET-II.5 with experimental data on net–baryon distributions. We get roughly for all of these probabilities values around 0.5. The definitions of these parameters and their default values in DPMJET-II.5 are given in the companion paper [1].

D. Realization of the intranuclear cascade process

Nothing has been changed in DPMJET-II.5 against DPMJET-II.3/4 with respect to the formation zone intranuclear cascade, nuclear evaporation and fragmentation, γ deexcitation of the residual nuclei and the Cronin effect. All of this was described in detail in [5,29,30].

E. Production of strange particles

Studies of strangeness production within this model were given in [35,37,38]. Enhanced generation of strange particles, in particular of strange antibaryons, has been proposed as a signal for the formation of quark gluon plasma in dense hadronic matter [87,88]. Recent data from experiments at the CERN SPS have already been interpreted within this scheme. However, we find it worthwhile to pursue the study of tested conventional models without QGP formation like the DPM before drawing final conclusions. The DPM is an independent string model. Since the individual strings are universal building blocks of the model, the ratio of *produced* strange particles over non-strange ones will be approximately the same in all reactions. However, since some strings contain sea quarks at one or both ends and since strange quarks are present in the proton sea, it is clear, that, by increasing the number of those strings, the ratio of strange over non-strange particles will increase. This will be the case for instance, when increasing the centrality in a nucleus-nucleus collision. It is obvious, that the numerical importance of the effect will depend on the assumed fraction of strange over non-strange quarks in the proton sea. The rather extreme case leading to a maximum increase of strangeness would be to assume a SU(3) symmetric sea (equal numbers of u , d and s flavors). We express the amount of SU(3) symmetry of the sea chain ends by our parameter s^{sea} defined as $s^{sea} = 2 \langle s_s \rangle / (\langle u_s \rangle + \langle d_s \rangle)$ where the $\langle q_s \rangle$ give the average numbers of sea quarks at the sea chain ends. Usually, DPMJET uses $s^{sea} = 0.5$.

There are a number of effects, which change the number of strange hadrons, especially strange and multistrange baryons and antibaryons in the model:

- (i) The presence of sea qq and $\bar{q}\bar{q}$ diquarks at sea-chain ends [89,90].
- (ii) The popcorn effect.
- (iii) The diquark breaking diagrams discussed in Section II.C, see also [51,52,85].
- (iv) The secondary interactions of co-moving produced particles [91,92], see also Section II.G.
- (v) Effects of string fusion [93,94] and percolation of strings [95,96].

It is certainly beyond the scope of the present paper, to discuss all of these effects in detail. The effects (i) to (iv) are contained in DPMJET-II.5.

F. Single diffractive cross sections in hadron-nucleus and nucleus-nucleus collisions

Let us first summarize the sampling of single diffractive events in DPMJET in hadron-hadron collisions.

Single diffraction within the Dual Parton Model was studied in detail and compared to experimental data in [36,76]. Single diffraction dissociation is represented by a triple-Pomeron exchange (high mass single diffraction) and a low mass component (low mass single diffraction) [15].

Diffractive processes characterized by the excitation of an initial hadron to intermediate resonances (low mass diffractive interactions) are introduced via a two channel eikonal formalism.

High mass single diffractive events are sampled cutting the triple-Pomeron graph. The excited system consists of two chains stretched between the constituents of the excited hadron and a $\bar{q}\bar{q}$ -pair of the Pomeron emitted from the hadron at the upper vertex.

Corresponding to $M_D^2 = x_D s$ and to the known $1/M_D^2$ -behaviour of the diffractive differential cross section $d^2\sigma_{sd}/dt dM_D^2$ we sample the sum of the momentum fractions of the $\bar{q}\bar{q}$ -pair $x_D = x_q + x_{\bar{q}}$ from a $1/x_D$ -distribution. Assuming that inelastic diffraction dissociation puts virtual hadronic states on the mass shell we limit this selection by the coherence condition.

$$M_D^2/s \leq (m_p R)^{-1} \quad \text{with} \quad R \simeq m_\pi^{-1} \quad (2.6)$$

where \sqrt{s} is the c.m. energy of the collision and R is the interaction radius.

An excited low mass single diffractive event is represented by a chain connected to the valence partons of one hadron. The invariant mass M_D is fixed in the same way as above.

We turn to single diffractive cross sections in hadron-nucleus and nucleus-nucleus collisions.

In DPMJET the simple approximation is used: single diffraction in nuclear collisions occurs only in Glauber collisions with only one participant of projectile as well as target ($N_A = N_B = N = 1$). In such collisions also the total number N of Glauber collisions is equal to one. In the first step of the $N_A = N_B = N = 1$ collision we have just a single hadron–hadron collision, single diffraction occurs, if this single collision is a diffractive collision. In the second step of the single diffractive hadron–nucleus or nucleus–nucleus collision we have the formation zone cascade in the participating nuclei followed by nuclear evaporation. There might be single diffractive collisions also in Glauber collisions with N larger than one. In such cases it is rather unlikely, that all collisions will be diffractive. If we have one single diffractive collision together with one or several nondiffractive collisions, the event just looks like a nondiffractive one. We neglect in DPMJET the small fraction of diffractive events, where all of these Glauber collisions are diffractive.

DPMJET allows in hadron–nucleus and nucleus–nucleus collisions like in hadron–hadron collisions to chose all collisions or only nondiffractive or only diffractive collisions. DPMJET always calculates the fraction of diffractive collisions to the inelastic cross section.

In Fig.12 we plot the single diffractive cross sections in proton–nucleus collisions as function of the nuclear mass number A . The single diffractive cross sections given are always for diffraction on the target as well as the projectile side. As to be expected we find $\sigma_{SD}^{h-A} \approx A^{1/3}$. Single diffractive nucleus–nucleus cross sections σ_{SD}^{A-B} are found to be rather similar to the h-Max(A,B) diffractive cross sections. In Table 3 we give only some examples of single diffractive nucleus–nucleus cross sections obtained from DPMJET-II.5.

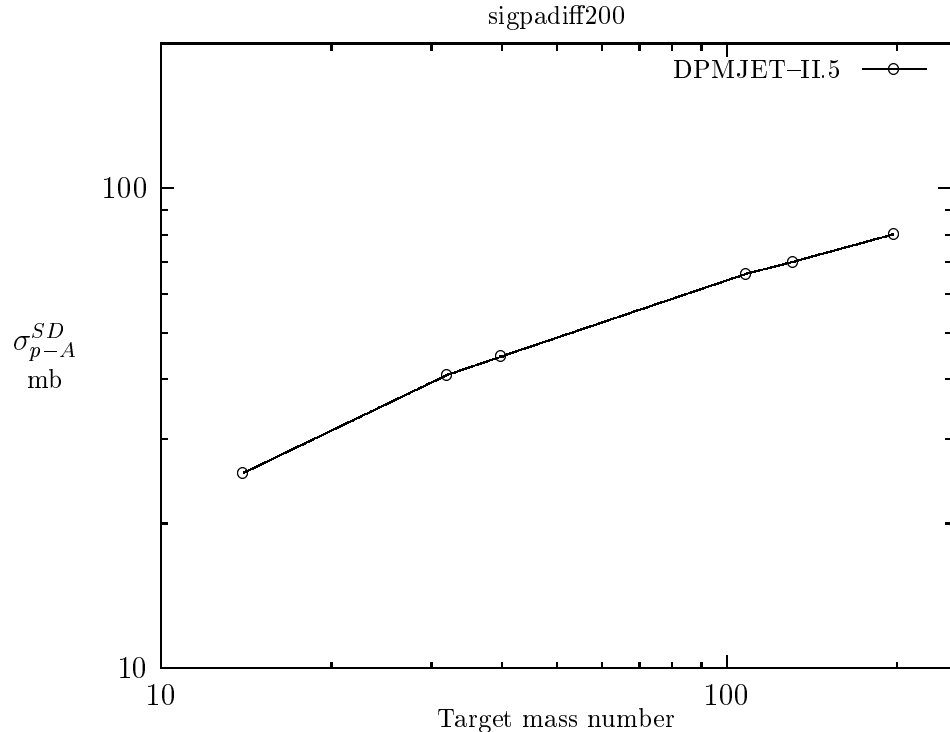


FIG. 12. Single diffractive cross sections calculated with DPMJET-II.5 in proton–nucleus collisions. The single diffractive cross sections given are for diffraction on the target as well as the projectile side.

Table 3. Diffractive cross sections in nucleus–nucleus collisions (in mb). The single diffractive cross sections given are for diffraction on the target as well as the projectile side.

Reaction	σ_{SD}^{A-B}
S–S	50.5
S–Ag	60.9
S–Au	67.6
Pb–Pb	72.8

G. Final state interactions of co-moving secondaries in nuclear collisions

Analyzing the rapidity distributions of produced Λ and $\bar{\Lambda}$ particles in central heavy ion collisions at CERN-SPS energies within the Dual Parton Model Capella et al [91,92] noted the need for secondary interactions of co-moving secondaries to understand the data. They only introduced the following secondary interactions



and



A reasonable cross section for these reactions of $\sigma \approx 1.5$ mb was needed in [91,92] to understand the data. All of this was done in [91,92] using analytical methods, not a Monte Carlo event generator. Final state interactions of co-moving secondaries was also used in [97,98] to explain the J/ψ suppression in Pb-Pb collisions.

The method of Capella et al [91,92] was implemented in DPMJET already in 1995. In DPMJET the method is used to modify the Monte Carlo events and we use only a cross section of $\sigma \approx 1.0$ mb. First results reproducing essentially the results of [91,92] are described shortly in [3] and in more detail in an unpublished code write-up [4]. We would like to stress, this method as implemented with only the two reactions given above, can only be considered as a first preliminary step. A better method of final state interactions should be implemented as a Monte Carlo method from the beginning and more types of secondary interactions should be taken into account including the reverse reactions. With the present method we can not expect to obtain reasonable results in situations with much higher secondary particle densities than in the heavy ion collisions at the CERN-SPS energy. Therefore, it is not recommended to use the secondary interaction option of DPMJET at RHIC or CERN-LHC energies.

H. Central nucleus-nucleus collisions in DPMJET

The sampling of a Glauber event according to the method of [77] proceeds as follows: First the impact parameter B of the hadron-nucleus or nucleus-nucleus collision is sampled from a distribution determined at the beginning by a Monte Carlo method. In a second step the number of interacting projectile and target nucleons $N_A = N_p$ and $N_B = N_t$ and the total number of Glauber collisions N are sampled.

We might define in DPMJET a central collision by different methods:

- (i) Allowing only impact parameters $B \leq B_{thr}$.
- (ii) Demanding, that a certain minimum fraction of the projectile or target nucleons takes part in the collision for instance $N_A = N_p \geq \alpha A$, where α is a number not far from unity.

Experiments investigating central nucleus-nucleus collisions are usually not able to determine reliably the impact parameters of the collisions. They might be able to determine the number of interacting projectile nucleons, for instance using a zero-degree calorimeter. Most often one finds however the central collision characterized by giving which fraction $F_{central}$ of all events are contained in the sample of most central collisions considered.

In order to keep contact to the $F_{central}$ definition we proceed in DPMJET in an iterative way. DPMJET is run rejecting all events with $N_A = N_p \leq \alpha A$ for a given α . At the same time we keep track which fraction of the events f_α is accepted in the run. α is iterated until $f_\alpha \approx F_{central}$.

I. Restrictions of DPMJET-II

DPMJET-II.5 works for hadron-hadron and hadron-nucleus collisions above 50 MeV kinetic energy, it has been compared to data on average multiplicities down to about 1 GeV and to data on Feynman x distributions down to 3-4 GeV see [4]. The HADRIN model used by DPMJET for hadron-hadron collisions below 5 GeV was compared to data down to several hundred MeV [99,100]. DPMJET-II.5 works for nucleus-nucleus interactions above 5 GeV per nucleon, but was never compared to experimental data below 60 GeV.

DPMJET-II.5 is able to run up to energies of approximately 10^{21} eV in the lab system (or $\sqrt{s} = 2000$ TeV).

III. COMPARING DPMJET-II.5 TO DATA

A. Comparing to data in hadron–hadron collisions

Before a model like DPMJET-II.5 can be used for anything, we have to demonstrate, that the model describes well enough the available data up to the highest energies. The parameters of the model as given in Table 1 are different from the parameters used in the previous version of the model, therefore, this agreement to the data is not trivial, even if the previous DPMJET version was quite successful in this respect.

Table 4. Comparison of average multiplicities of produced hadrons in proton– proton collisions at 200 GeV. The experimental data are from Ref. [101].

Particle	DPMJET-II.5	Exp. [101]
n_{ch}	7.69	7.69 ± 0.06
n_-	2.85	2.85 ± 0.03
p	1.24	1.34 ± 0.15
n	0.68	0.61 ± 0.30
π^+	3.25	3.22 ± 0.12
π^-	2.58	2.62 ± 0.06
π^0	3.55	3.34 ± 0.24
K^+	0.30	0.28 ± 0.06
K^-	0.19	0.18 ± 0.05
K_S^0	0.23	0.17 ± 0.01
Λ	0.14	0.096 ± 0.01
$\bar{\Lambda}$	0.0178	0.0136 ± 0.004
ρ^0	0.48	0.33 ± 0.06
\bar{p}	0.048	0.05 ± 0.02

We start with looking at data, which prove, that the average multiplicity and the particle content are well described. In Table 4 we compare to the very well known multiplicities of secondary hadrons in 200 GeV p–p collisions from Ref. [101]. In Table 5 we compare to multiplicities of secondary hadrons and hadron resonances in $\sqrt{s} = 27.5$ GeV p–p collisions from Ref. [102].

Table 5. Comparison of average multiplicities of produced hadrons and hadron resonances in proton– proton collisions at $\sqrt{s} = 27.5$ GeV. The experimental data are from Ref. [102].

Particle	DPMJET-II.5	Exp. [102]
p	1.28	$1.20 \pm 0.097 \pm 0.022$
π^+	3.52	$4.10 \pm 0.11 \pm 0.15$
π^-	2.87	$3.34 \pm 0.08 \pm 0.12$
π^0	3.88	$3.87 \pm 0.12 \pm 0.16$
K^+	0.34	$0.331 \pm 0.016 \pm 0.007$
K^-	0.24	$0.224 \pm 0.011 \pm 0.004$
K_S^0	0.27	$0.232 \pm 0.011 \pm 0.004$
Λ	0.156	$0.125 \pm 0.008 \pm 0.008$
$\bar{\Lambda}$	0.026	$0.020 \pm 0.004 \pm 0.0008$
Σ^+	0.050	$0.048 \pm 0.015 \pm 0.004$
Σ^-	0.016	$0.0128 \pm 0.0061 \pm 0.0032$
Δ^{++}	0.24	$0.218 \pm 0.0031 \pm 0.013$
Δ^0	0.23	$0.141 \pm 0.0098 \pm 0.0089$
$\bar{\Delta}^{++}$	0.005	$0.013 \pm 0.0049 \pm 0.0049$
$\bar{\Delta}^0$	0.006	$0.0336 \pm 0.008 \pm 0.0006$
ρ^0	0.54	$0.385 \pm 0.018 \pm 0.038$
ρ^+	0.54	$0.552 \pm 0.083 \pm 0.046$
ρ^-	0.43	$0.355 \pm 0.058 \pm 0.033$
ω	0.50	$0.390 \pm 0.024 \pm 0.002$
η	0.55	$0.30 \pm 0.02 \pm 0.054$
K^{*+}	0.18	$0.132 \pm 0.016 \pm 0.002$
K^{*-}	0.11	$0.088 \pm 0.012 \pm 0.001$
K^{*0}	0.15	$0.119 \pm 0.021 \pm 0.002$
\bar{K}^{*0}	0.11	$0.0903 \pm 0.016 \pm 0.001$
ϕ	0.029	$0.019 \pm 0.0018 \pm 0.054$
\bar{p}	0.066	$0.063 \pm 0.002 \pm 0.001$

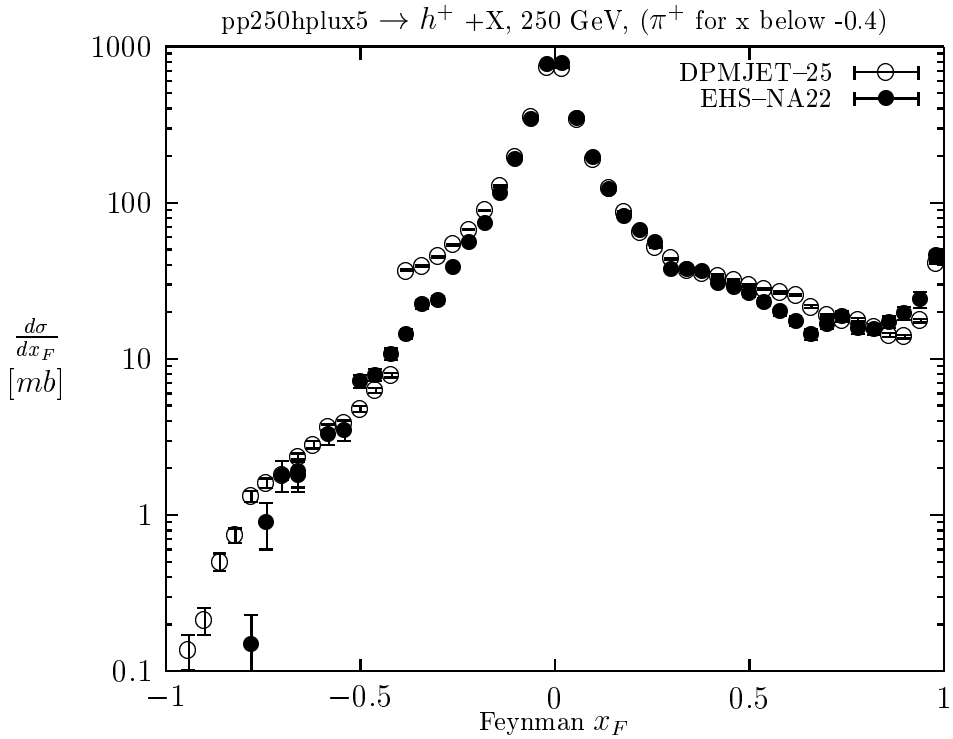


FIG. 13. Comparison of Feynman- x distributions of positively charged hadrons produced in proton–proton collisions at 250 GeV. The experimental data are from the EHS–NA22 Collaboration [103].

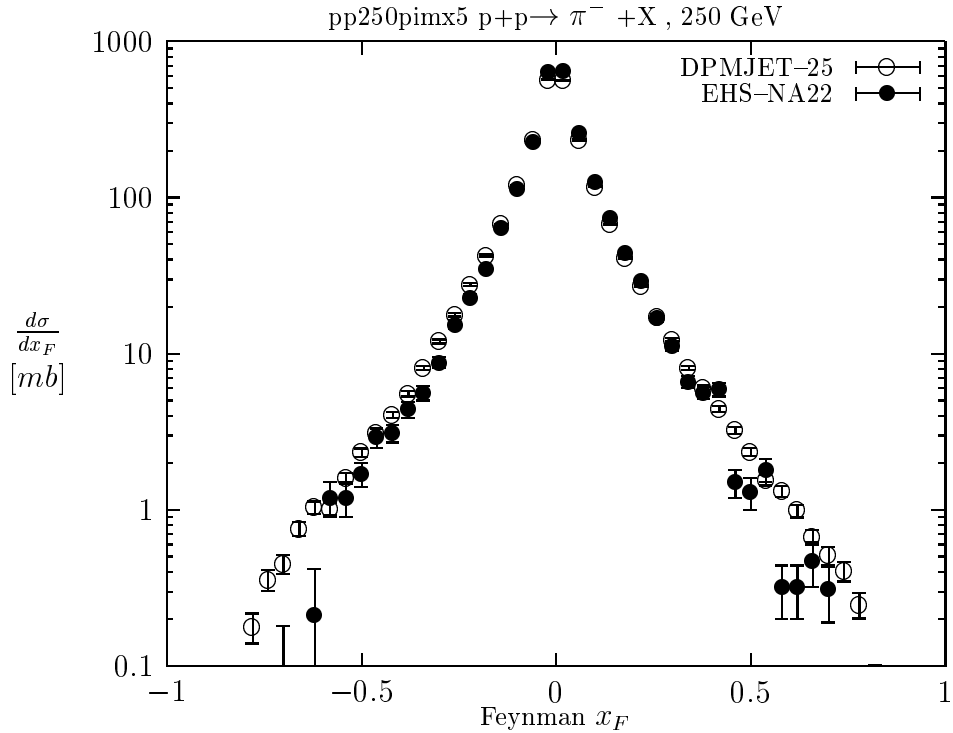


FIG. 14. Comparison of Feynman- x distributions of π^- mesons produced in proton–proton collisions at 250 GeV. The experimental data are from the EHS–NA22 Collaboration [103].

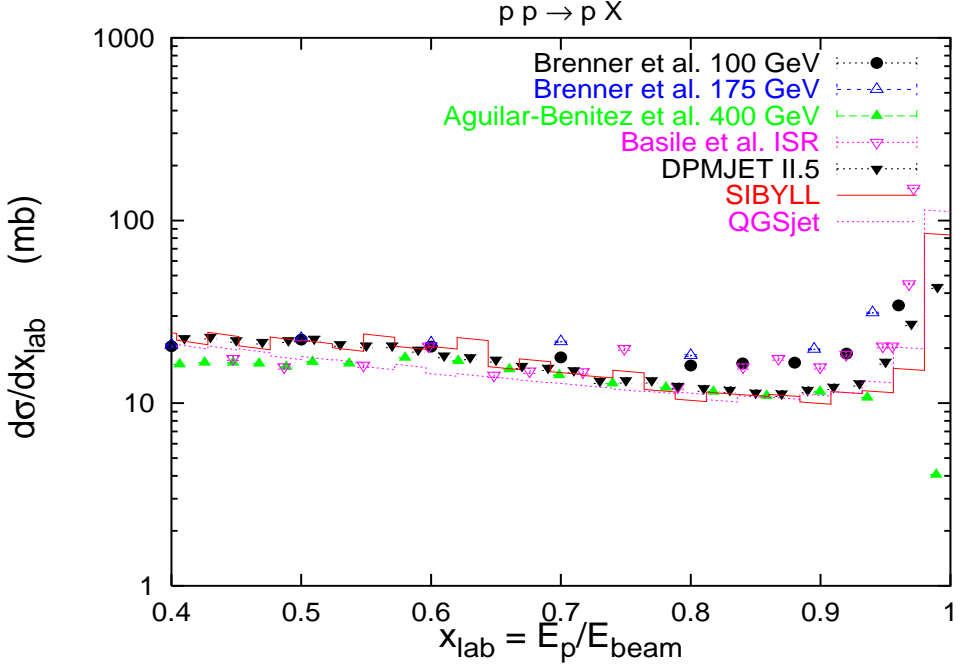


FIG. 15. x_{lab} cross sections in p-p collisions. We compare data at different energies [104,102,105] shown as symbols with DPMJET-II.5 at $p_{lab} = 200$ GeV/c shown as solid triangles. The data are also compared to the SIBYLL [106] and QGSJET [107] models shown as histograms.

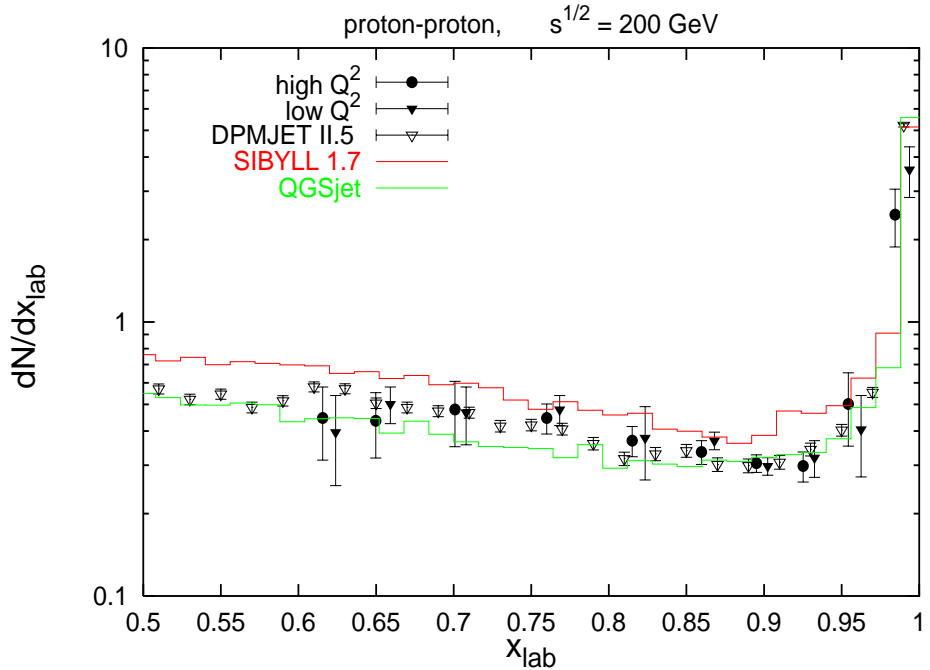


FIG. 16. Energy fraction x_{lab} carried by the leading proton. The data are photoproduction and DIS measurements at $\sqrt{s} = 200$ GeV [108,109] shown as symbols compared to DPMJET-II.5 for p-p collisions at $\sqrt{s} = 200$ GeV shown as open triangles. The data are also compared to the SIBYLL [106] and QGSJET [107] models shown as histograms.

In Fig. 13 and 14 we compare the model with NA-22 data on the Feynman- x distribution of positively charged hadrons and of π^- produced in 250 GeV pp collisions. In Fig. 13 we observe in particular (compared to previous DPMJET versions) a better agreement of the model predictions with the forward production of protons.

Distributions of leading protons are compared more directly to data in the following two Figs. 15 and 16. The Figs. are adopted from talks of Engel [110,111]. But of course, we present now the DPMJET-II.5 results. The leading particle production is very important for the Cosmic Ray cascade simulation.

In Fig. 15 we compare x_{lab} cross sections in p - p collisions measured at different energies [104,102,105] with DPMJET-II.5 results at $p_{lab} = 200$ GeV/c. The DPMJET cross sections change only very slowly with energy. The obtained agreement with DPMJET-II.5 to the data is much better than with former DPMJET versions see [110]. The data are also compared to the SIBYLL [106] and QGSJET [107] models.

In Fig. 16 we compare the energy fraction x_{lab} carried by the leading proton. The data are photoproduction and DIS measurements from the HERA Collider at $\sqrt{s} = 200$ GeV [108,109]. We compare to DPMJET-II.5 for p - p collisions at $\sqrt{s} = 200$ GeV. The forward production of leading protons is not expected to depend strongly on the reaction channel. It is found again, that DPMJET-II.5 agrees much better to the data than older DPMJET versions, see [111]. This comparison demonstrates, that the leading proton distribution at $\sqrt{s} = 200$ GeV is still rather flat like at the much lower energies in Fig. 15. At $\sqrt{s} = 200$ GeV both versions of DPMJET-II.5 with GSQBS and USQBS and with only GSQBS, (discussed in Section II) lead still to very similar x_{lab} distributions of secondary protons. Unfortunately therefore, these data cannot be used to discriminate between the two DPMJET-II.5 versions. The data are also compared to the SIBYLL [106] and QGSJET [107] models.

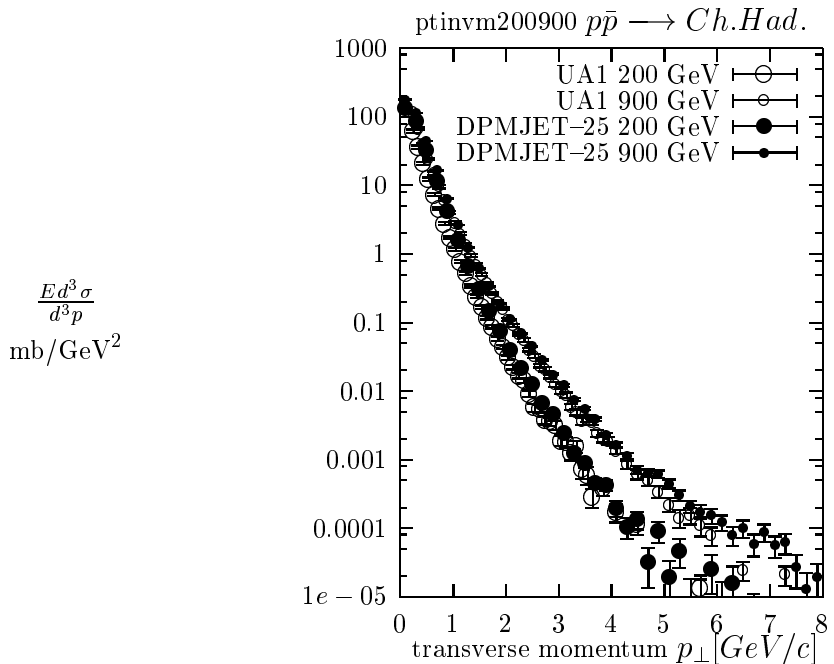


FIG. 17. Comparison with transverse momentum cross sections at $\sqrt{s} = 0.2$ and $.9$ TeV with collider data from the UA-1 Experiment [112].

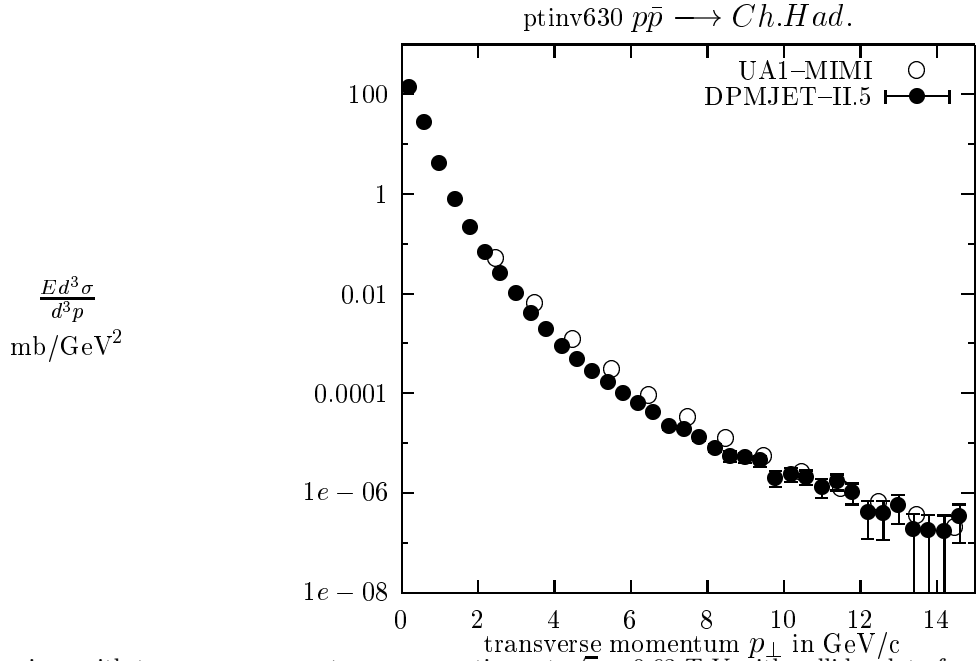


FIG. 18. Comparison with transverse momentum cross sections at $\sqrt{s} = 0.63$ TeV with collider data from the UA-1 MIMI Collaboration [113]. The experimental data are represented by the parametrization given by the Experiment.

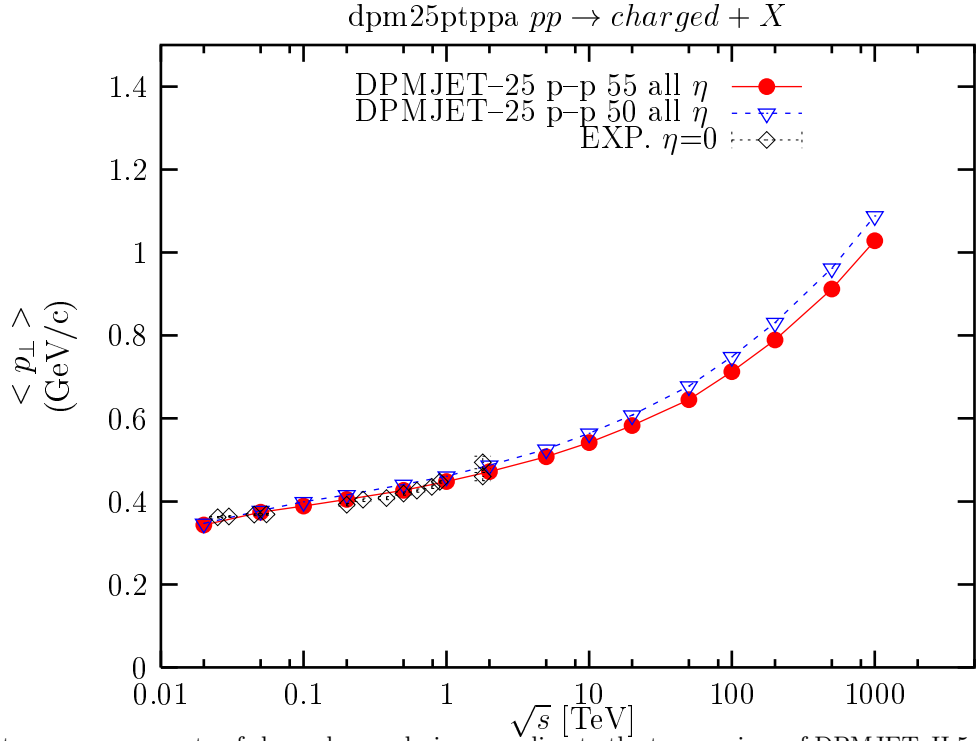


FIG. 19. Average transverse momenta of charged secondaries according to the two versions of DPMJET-II.5 produced in pp collisions in the full pseudorapidity interval as function of the center of mass energy \sqrt{s} . We compare to data collected by the UA-1 Collaboration [112] which refer to the central pseudorapidity range and are therefore expected to be slightly larger than in the full range.

Hadron transverse momentum distributions were measured by the UA-1 Collaboration [112]. In Fig.17 we compare the distributions at $\sqrt{s} = 200$ GeV and 900 GeV with DPMJET-II.5. The transverse momentum distribution up to larger p_{\perp} was determined by the UA-1-MIMI Collaboration [113]. In Fig.18 we compare the model results with the parametrization of the data given by this experiment.

In Fig.19 we compare average transverse momenta as obtained from the two versions discussed in Section II of DPMJET-II.5 as function of the cms energy \sqrt{s} with data collected by the UA-1 Collaboration. This plot gives at the same time the DPMJET-II.5 predictions for the average transverse momenta up to $\sqrt{s} = 1000$ TeV. We find, that the average transverse momenta in both versions of the model agree rather well to each other. Average transverse momenta depend on the longitudinal variables, they differ if one chooses different pseudorapidity ranges, the data given for the central pseudorapidity range are expected to be slightly larger than the calculation given for the full range.

With rising energy the fraction of strange hadrons rises slowly. In Fig.20 the K/π ratio according to DPMJET-II.5 for pp or $p\bar{p}$ collisions is compared to data from the E735 Collaboration [114].

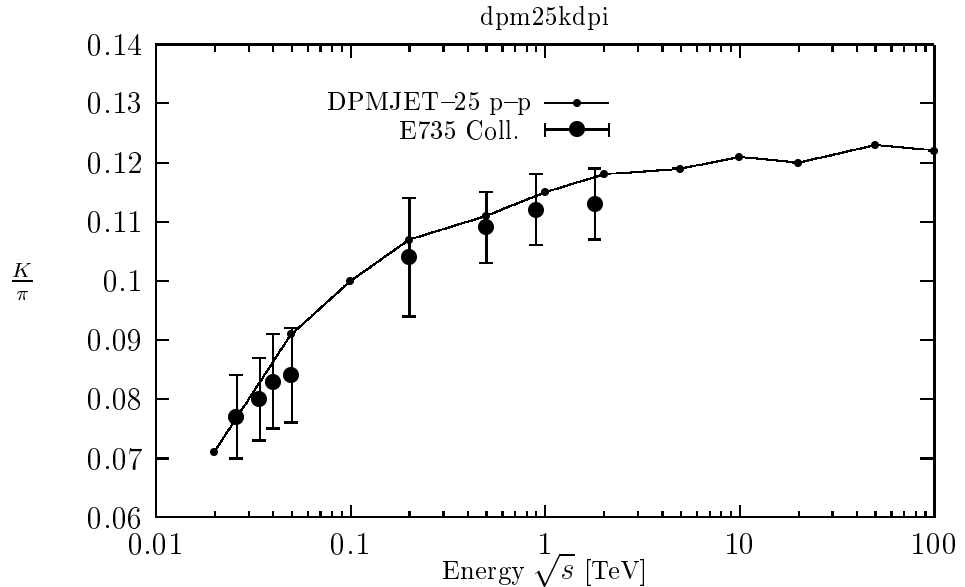


FIG. 20. K/π ratios in pp or $p\bar{p}$ collisions as function of the cms energy \sqrt{s} . The DPMJET-II.5 calculation is compared with data collected from the E735 Collaboration at Fermilab [114].

B. Comparing to data in hadron–nucleus and nucleus–nucleus collisions

We now turn to collisions with nuclei.

In Table 6 we compare average multiplicities of negatively charged hadrons calculated with DPMJET-II.5 in hadron–hadron, minimum bias hadron–nucleus and central nucleus–nucleus collisions with experimental data.

Table 6. Comparison of average multiplicities of produced negatively charged hadrons in proton–proton, minimum bias proton–nucleus and central nucleus–nucleus collisions at 200 GeV.

Collision	DPMJET-II.5	Exp.	Reference
p–p	2.85	2.85 ± 0.03	[101]
p–S	5.10	5.0 ± 0.2	[115]
p–Ar	5.30	5.39 ± 0.17	[116]
p–Ag	6.18	6.2 ± 0.2	[117]
p–Xe	6.43	6.84 ± 0.13	[116]
p–Au	6.81	7.0 ± 0.4	[117]
p–Au	6.81	7.3 ± 0.3	[118]
S–S central	103	98 ± 3	[49]
S–Ag central	174	186 ± 11	[49]
S–Au central	202	225 ± 12	[49]

Table 7. Comparison of average multiplicities of produced strange hadrons in central S–S and S–Ag collisions at 200 GeV. For DPMJET-II.5 we give the results for the models without and with secondary interactions of comovers and it is assumed that Σ^0 and $\bar{\Sigma}^0$ have decayed. The experimental data are from the NA35 Collaboration [119].

Reaction	Particle	DPMJET-II.5	DPMJET-II.5 with sec.int.	Exp. [119]
S–S	Λ	5.7	7.3	9.4 ± 1.0
S–S	$\bar{\Lambda}$	1.13	1.22	2.6 ± 0.3
S–S	K_S^0	8.7	9.1	10.5 ± 1.7
S–S	K^+	10.6	11.4	12.5 ± 0.4
S–S	K^-	6.8	6.9	6.9 ± 0.4
S–Ag	Λ	9.6	13.1	15.2 ± 1.2
S–Ag	$\bar{\Lambda}$	1.8	2.0	2.6 ± 0.3
S–Ag	K_S^0	14.6	15.5	15.5 ± 1.5
S–Ag	K^+	17.8	19.7	17.4 ± 1.0
S–Ag	K^-	11.4	11.4	9.6 ± 1.0

In Tables 7 and 8 we give the average multiplicities of produced strange hadrons in central S–S, S–Ag and Pb–Pb collisions at 200 GeV (158 GeV for Pb–Pb). We give the DPMJET-II.5 results for the models without and with secondary interactions and it is assumed, that Σ^0 and $\bar{\Sigma}^0$ have decayed. The experimental data for central S–S and

S–Ag collisions are from the NA35 Collaboration [119]. There is some doubt, that the simple model for secondary interactions in DPMJET–II.5 gives correct results in a situation with such high produced hadron density like in the central Pb–Pb collisions.

In Table 8 we give the results for central Pb–Pb collisions also for the RHIC and LHC energies and we include charged multiplicities and central plateau heights in the Table. At the LHC DPMJET–II.5 gives a slightly lower plateau than DPMJET–II.2 (for which the plateau was given in [120]). The central plateaus at RHIC and LHC energies given in Table 8 agree however very well with the ones given by Capella in [85].

Table 8. Comparison of average multiplicities of produced strange hadrons in central Pb–Pb collisions at 158 GeV and at the energies of RHIC and the LHC. For DPMJET–II.5 we give only at 158 GeV the results for the models without and with secondary interactions of comovers and it is assumed that Σ^0 and $\bar{\Sigma}^0$ have decayed.

Particle	158 GeV DPMJET–II.5	158 GeV DPMJET–II.5 with sec.int.	RHIC	LHC
Λ	51	84	107	242
$\bar{\Lambda}$	11.9	14.6	54	181
K_S^0	70	79	359	1306
K^+	86	104	390	1359
K^-	54	56	341	1302
Ξ^-	3.81	3.80	10.0	24.2
$\bar{\Xi}^+$	1.67	1.64	6.0	19.1
Ω^-	0.24	0.24	0.9	2.2
$\bar{\Omega}^+$	0.18	0.17	0.7	1.9
$(dN^{ch}/dy^*)_{y^*=0}$	525	516	1282	2801
Fraction of cent. coll. (%)	5	5	3	4
h^-	828	807	3560	12581

In Fig. 21.a the comparison is with the rapidity distribution of negatively charged hadrons in p–p, p–Ar and p–Xe collisions at 200 GeV and in Fig. 21.b we compare to rapidity distributions of negatively charged hadrons in central S–S and S–Ag collisions.

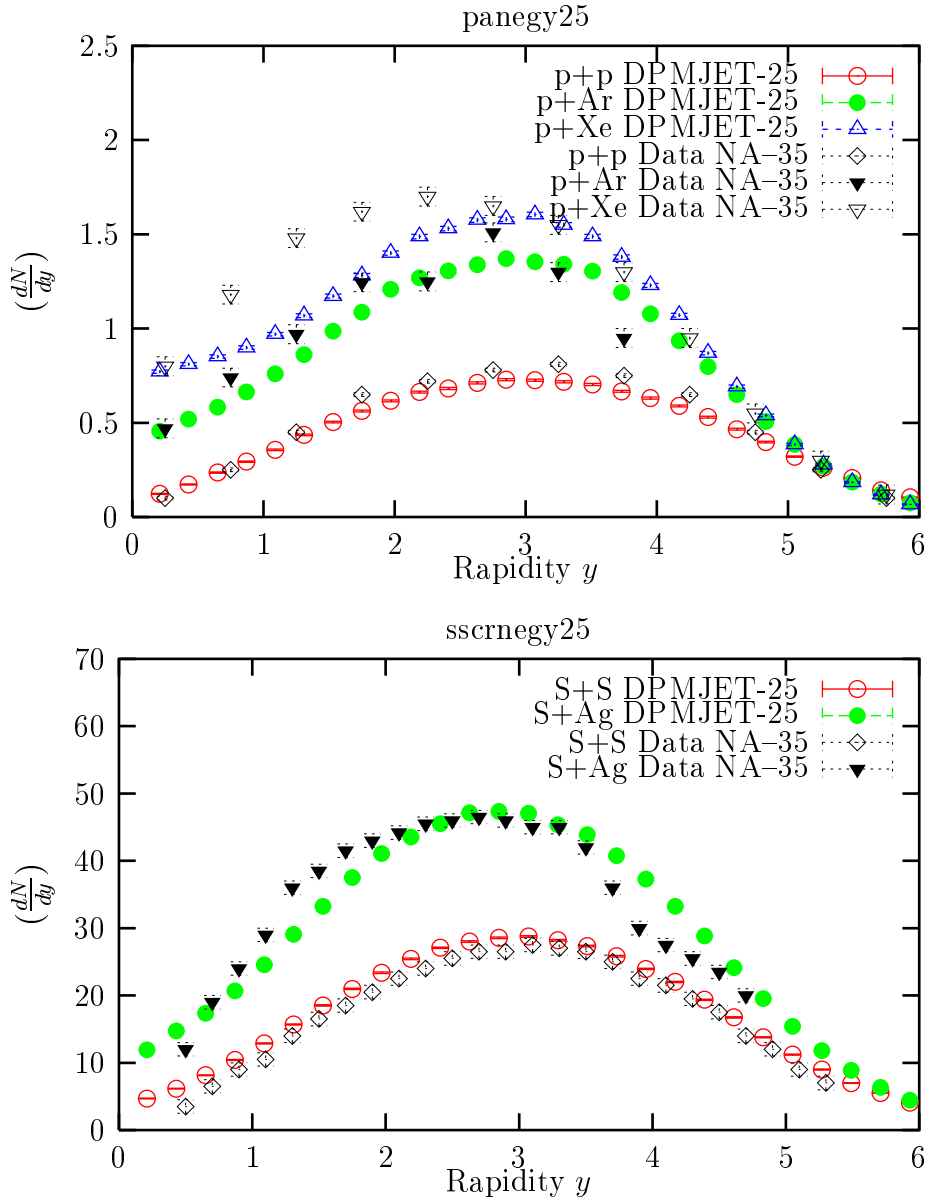


FIG. 21. (a) Negatively charged particle rapidity distribution for p-p, p-Ar and p-Xe interactions. The DPMJET-II.5 results are compared with data [49]. (b) Rapidity distribution of negatively charged hadrons in central S-S and S-Ag collisions. The results of DPMJET-II.5 are compared with data from the NA-35 Collaboration [49].

In Fig. 22 we compare rapidity distributions of π^+ , π^- , K^+ and K^- mesons produced in central (4%) Pb–Pb collisions at 158 AGeV/c. The experimental data, mainly in the central rapidity region are from the NA-44 Collaboration [121]. The agreement of model and data is encouraging, however not perfect.

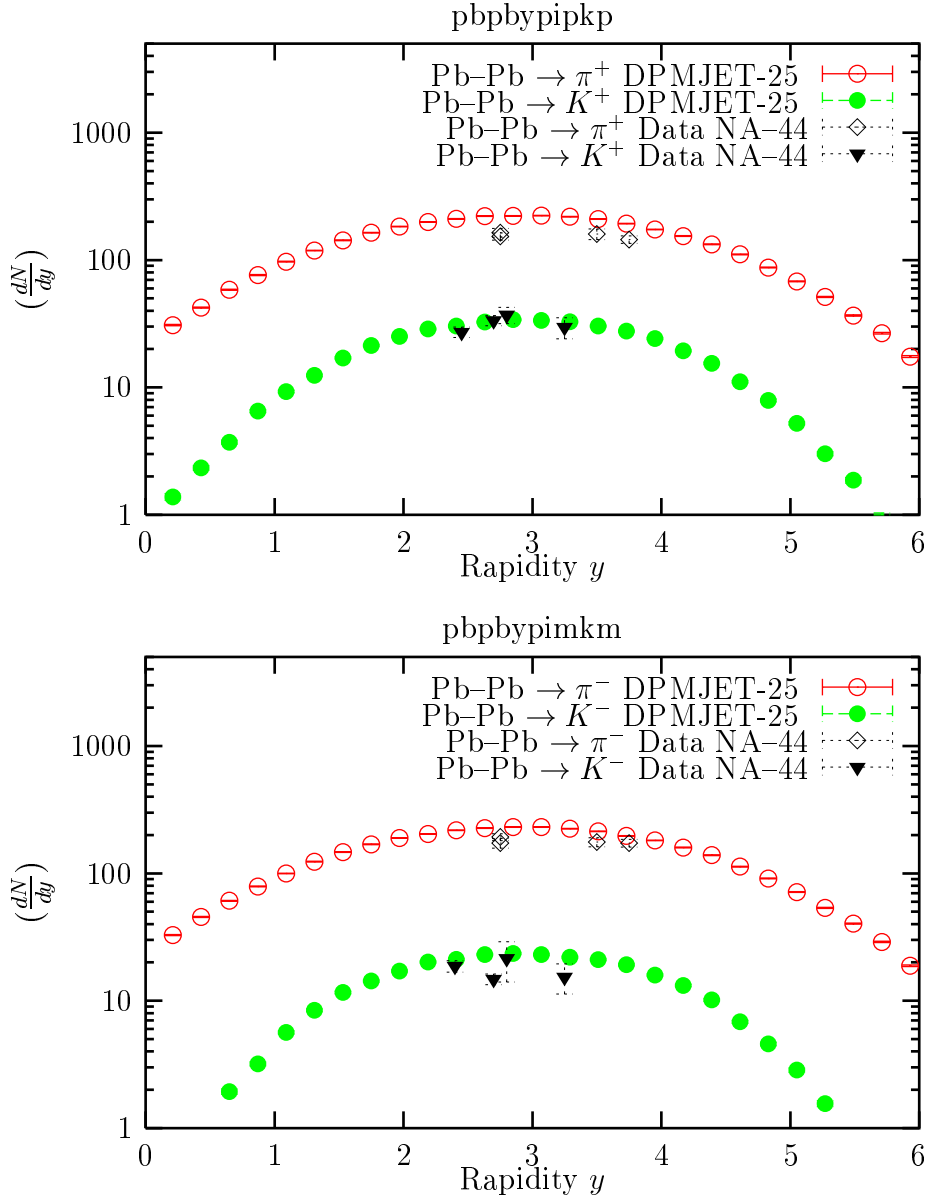


FIG. 22. (a) Rapidity distributions of π^+ and K^+ mesons produced in central Pb–Pb collisions. The DPMJET-II.5 distributions are compared with experimental data from the NA-44 Collaboration [121]. (b) Rapidity distributions of π^- and K^- mesons produced in central Pb–Pb collisions. The DPMJET-II.5 distributions are compared with experimental data from the NA-44 Collaboration [121].

C. Baryon stopping

We present first the DPMJET predictions at $p_{lab} = 200$ GeV/c for net baryon rapidity distributions in the original model without the new GSQBS and USQBS diagrams. In Fig. 23.a we present the leading net proton ($p - \bar{p}$) rapidity distribution $dN_p/dy - dN_{\bar{p}}/dy$ in p-p, p-S, central S-S and central Pb-Pb collisions. In Fig. 23.b we present the net Λ ($\Lambda - \bar{\Lambda}$) rapidity distribution $dN_{\Lambda}/dy - dN_{\bar{\Lambda}}/dy$ in p-p, p-S, central S-S and central Pb-Pb collisions. In p-p collisions, which at the given collision energy are hardly modified by the new GSQBS and USQBS diagrams, we observe a dip at central rapidity. This dip is also present in DPMJET without the new GSQBS and USQBS diagrams in p-S and central A-A collisions. This disagrees to the data presented in the next Figures.

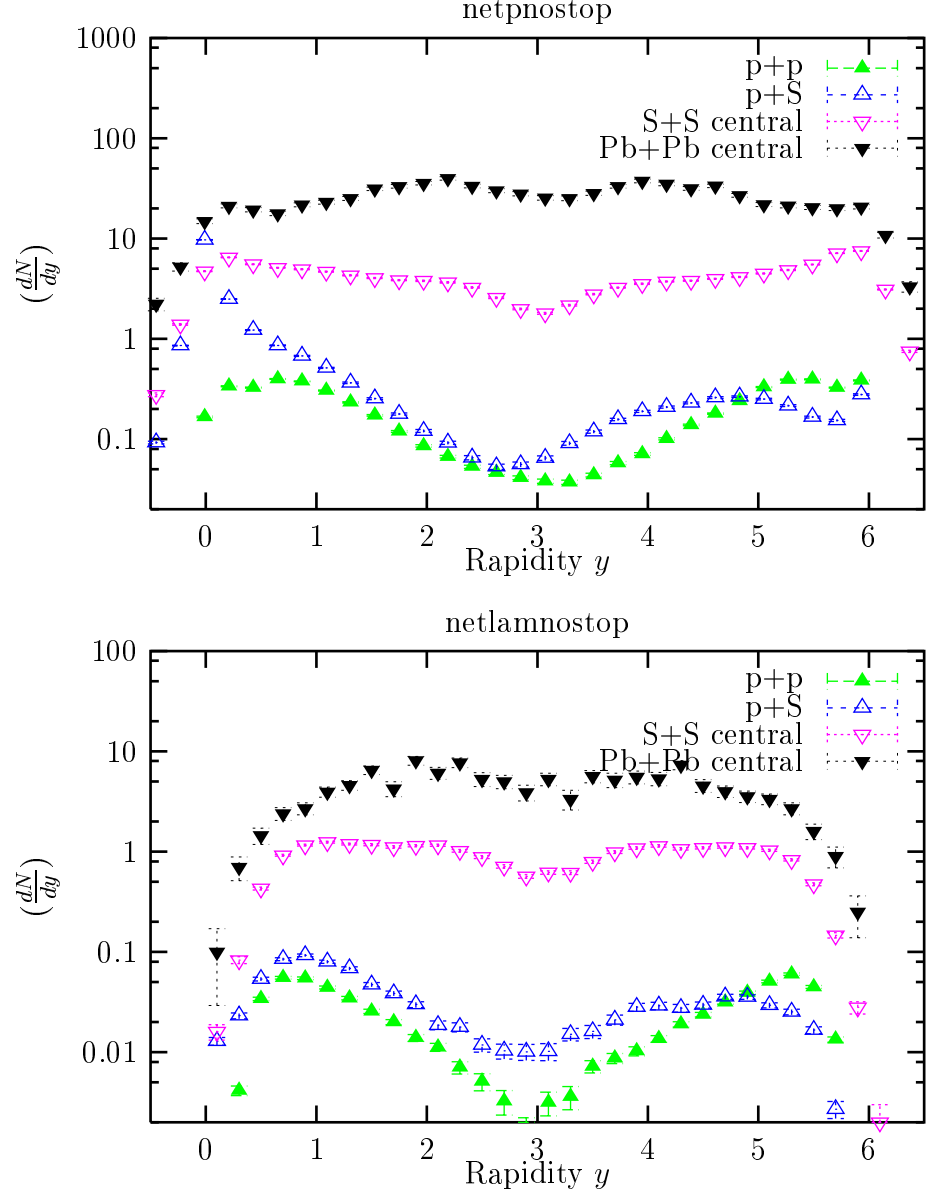


FIG. 23. (a) Net proton ($p - \bar{p}$) rapidity distribution in p-p, p-S, central S-S and central Pb-Pb. collisions. Calculated with DPMJET-II.5 without the new diagrams modifying baryon stopping. (b) Net Λ ($\Lambda - \bar{\Lambda}$) rapidity distribution in p-p, p-S, central S-S and central Pb-Pb. collisions. Calculated with DPMJET-II.5 without the new GSQBS and USQBS diagrams modifying baryon stopping.

In Fig. 24.a and 24.b we compare the net–proton distributions according to the full DPMJET–II.5 model with data in p–S and p–Au collisions [49]. Now the dips at central rapidity are filled in the model, we observe like in the data at central rapidity a flat net–proton rapidity distribution.

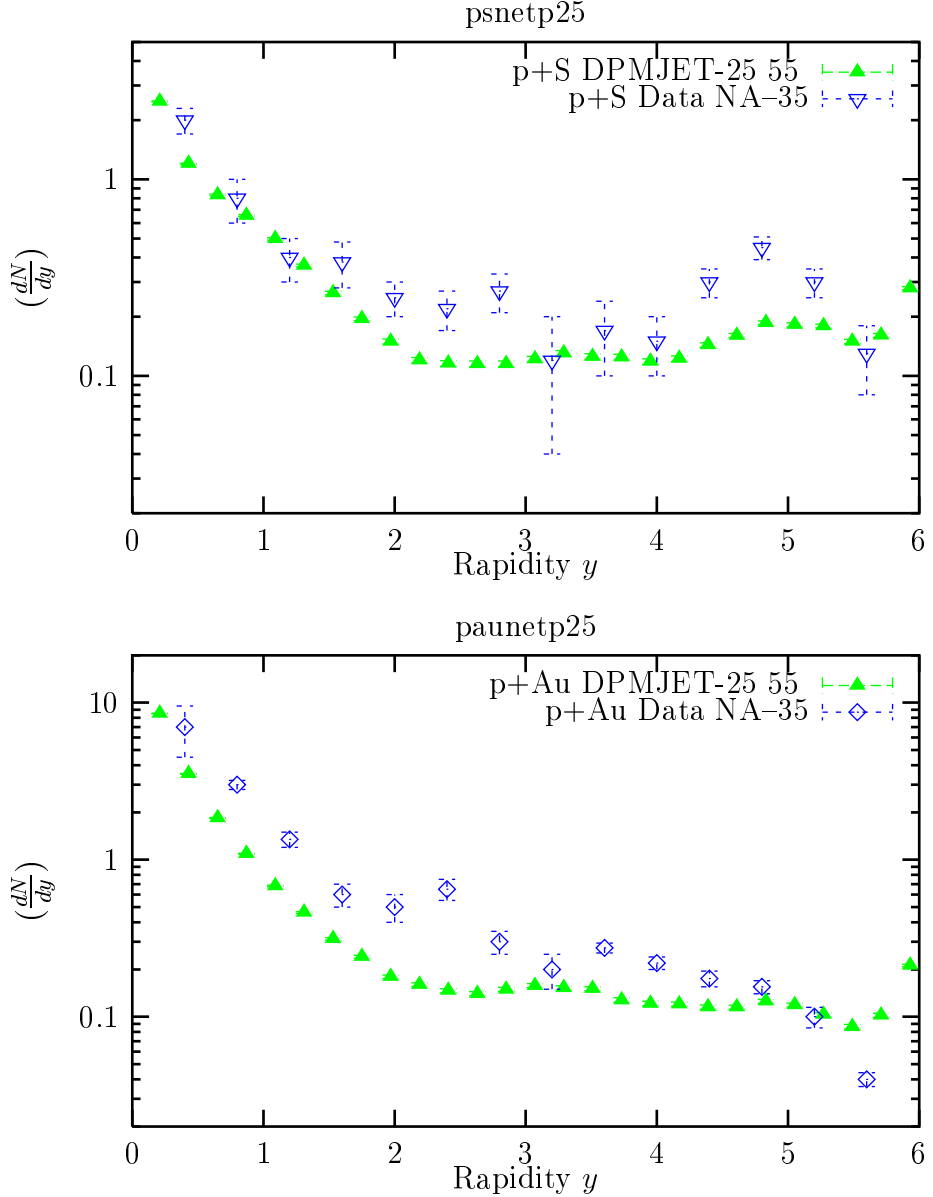


FIG. 24. (a) Net proton ($p - \bar{p}$) rapidity distribution in p–S collisions. The DPMJET–II.5 results are compared with data [49]. (b) Net proton ($p - \bar{p}$) rapidity distribution in p–Au collisions. The DPMJET–II.5 results are compared with data [49].

In Fig. 25 we compare the full DPMJET-II.5 model in the two versions without and with secondary interactions with data on net-proton production in central S-S collisions. Also here the dip at central rapidity in the model has disappeared (compare to Fig.23), however, the agreement to the data [49] is not perfect. There is a significant disagreement in the fragmentation regions of the two nuclei. The reason for this is in the spectator evaporation protons included in DPMJET, but apparently not in the data.

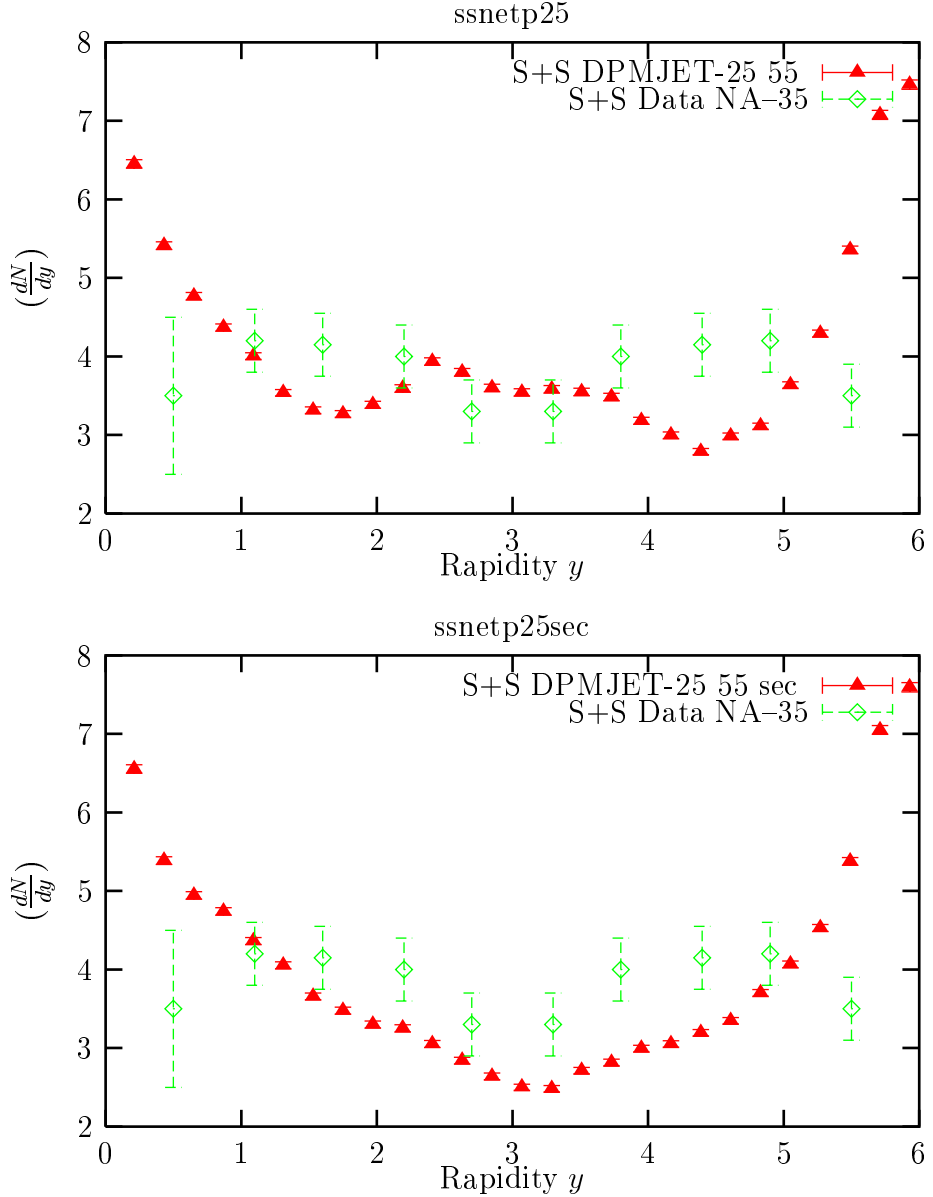


FIG. 25. Net proton ($p - \bar{p}$) rapidity distribution in central S-S collisions. The DPMJET-II.5 results are compared with data [49]. (a) DPMJET-II.5 without secondary interactions. (b) DPMJET-II.5 with secondary interactions.

In Fig. 26 we compare the full model to data on net- Λ production in p-S collisions. In Fig. 26 the dip at central rapidity has disappeared in the model. In Fig. 27.a and .b we compare the full model to data on net- Λ production central S-S collisions for the two models with and without secondary interactions. In Fig. 27.a and .b again the central dips in the models are largely reduced but the agreement to the NA35-data is rather unsatisfactory in the model without secondary interactions. Also the agreement of the model without secondary interactions to the total number of Λ 's produced according to NA35 is rather unsatisfactory, see Table 7. However, we find no disagreement to the total- Λ rapidity distribution as measured by Na36 [122].

We might conclude from the comparison of net-p and net- Λ production, that the secondary interaction is indeed needed to understand the data, further improvements to the secondary interactions might be useful.

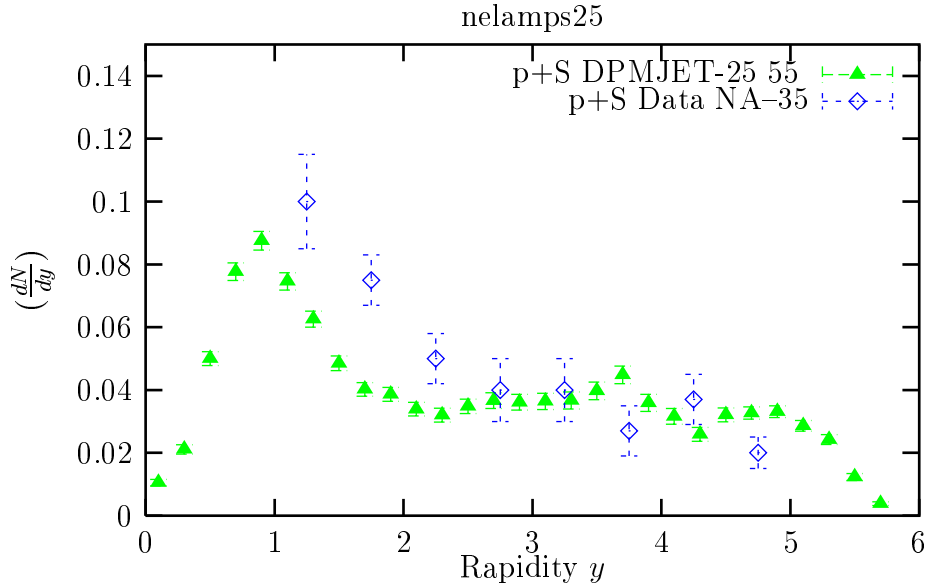


FIG. 26. Net Λ ($\Lambda - \bar{\Lambda}$) rapidity distribution in p-S collisions. The DPMJET-II.5 results are compared with data [49].

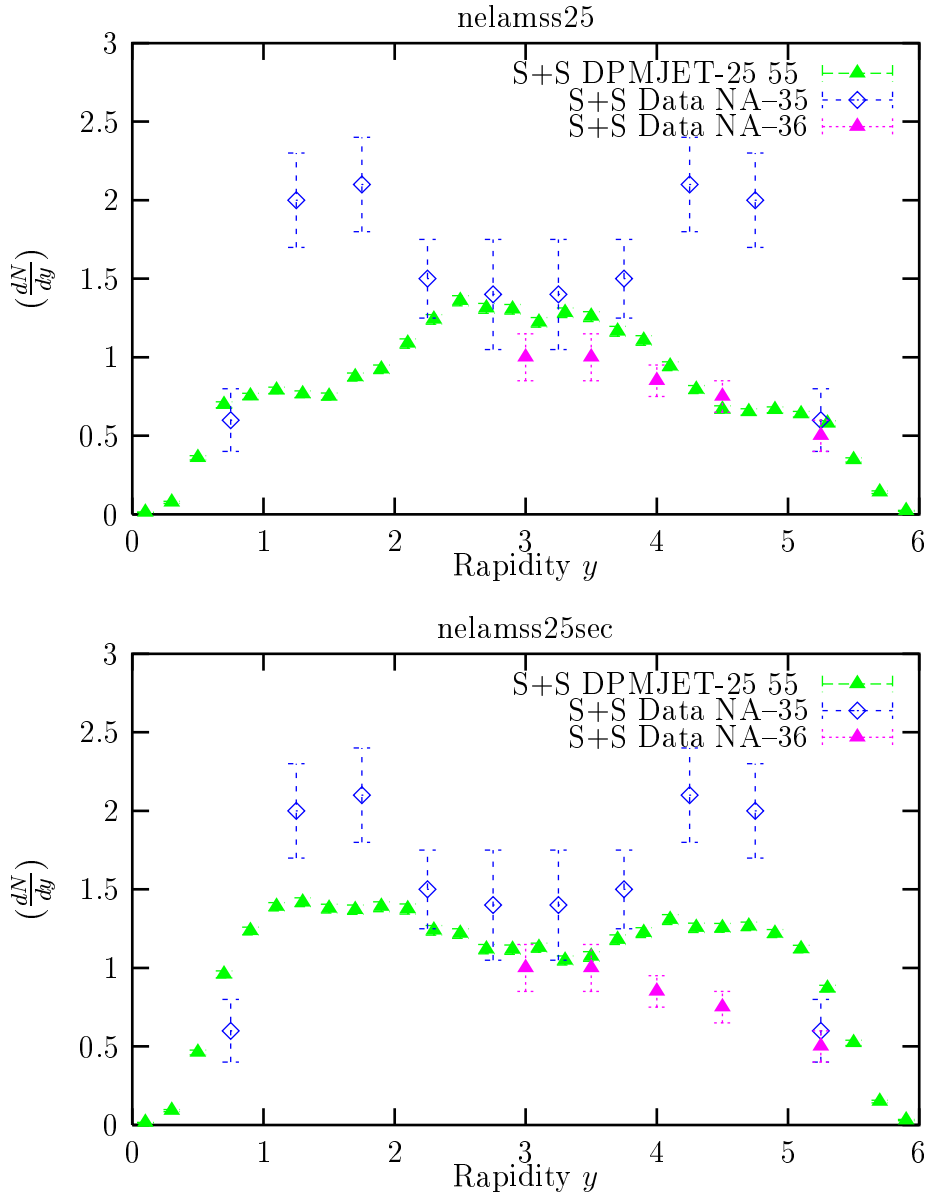


FIG. 27. Net Λ ($\Lambda - \bar{\Lambda}$) rapidity distribution in central S-S collisions. The DPMJET-II.5 results are compared with data from NA35 [49] and with the total Λ production as measured by NA36 [122]. **(a)** DPMJET-II.5 without secondary interactions. **(b)** DPMJET-II.5 with secondary interactions.

IV. PROPERTIES OF THE MODEL IN THE HIGHEST ENERGY REGION

In all plots in this Section we present the DPMJET-II.5 results for the two versions of the model discussed already in Section II.C:

(i)With only the new diagram for baryon stopping GSQBS, this version is characterized in the plots by 50, this version corresponds in its high energy behaviour approximately to the previous version of the model DPMJET-II.4.

(ii)With both new diagrams for baryon stopping GSQBS and USQBS, this version is characterized in the plots by 55, the hight energy behaviour of this version is new, at high energies the baryons carry 5 to 10 percent less energy than in version 50, correspondingly the mesons carry more energy than in version 50.

Fig.28 presents the rise of the total charged multiplicity in p-p and p-N collisions with the cms energy \sqrt{s} .

The corresponding rise of the average transverse momenta was already presented in Fig.19

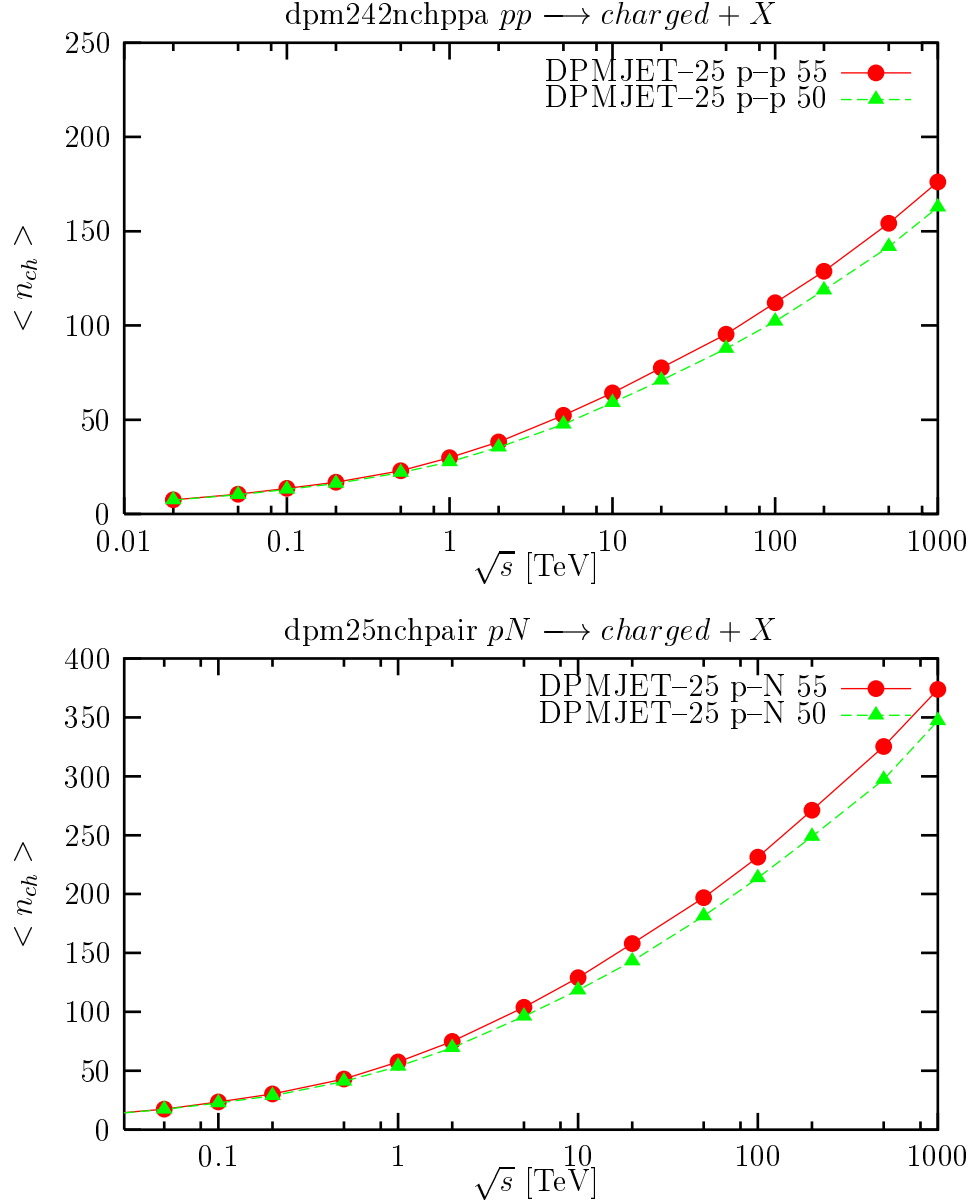


FIG. 28. Rise of the charged multiplicity in inelastic p-p and p-N collisions in the center of mass energy range between $\sqrt{s}=0.02$ TeV and $\sqrt{s} = 1000$ TeV.

Following for instance the basic discussion of [123], we introduce a variable x_{lab} similarly to Feynman- x_F , but this time in the lab-frame :

$$x_{lab} = \frac{E_i}{E_0} \quad (4.1)$$

E_i is the lab-energy of a secondary particle i and E_0 is the lab-energy of the projectile in a h-nucleus collision. We introduce x_{lab} distributions $F(x_{lab})$:

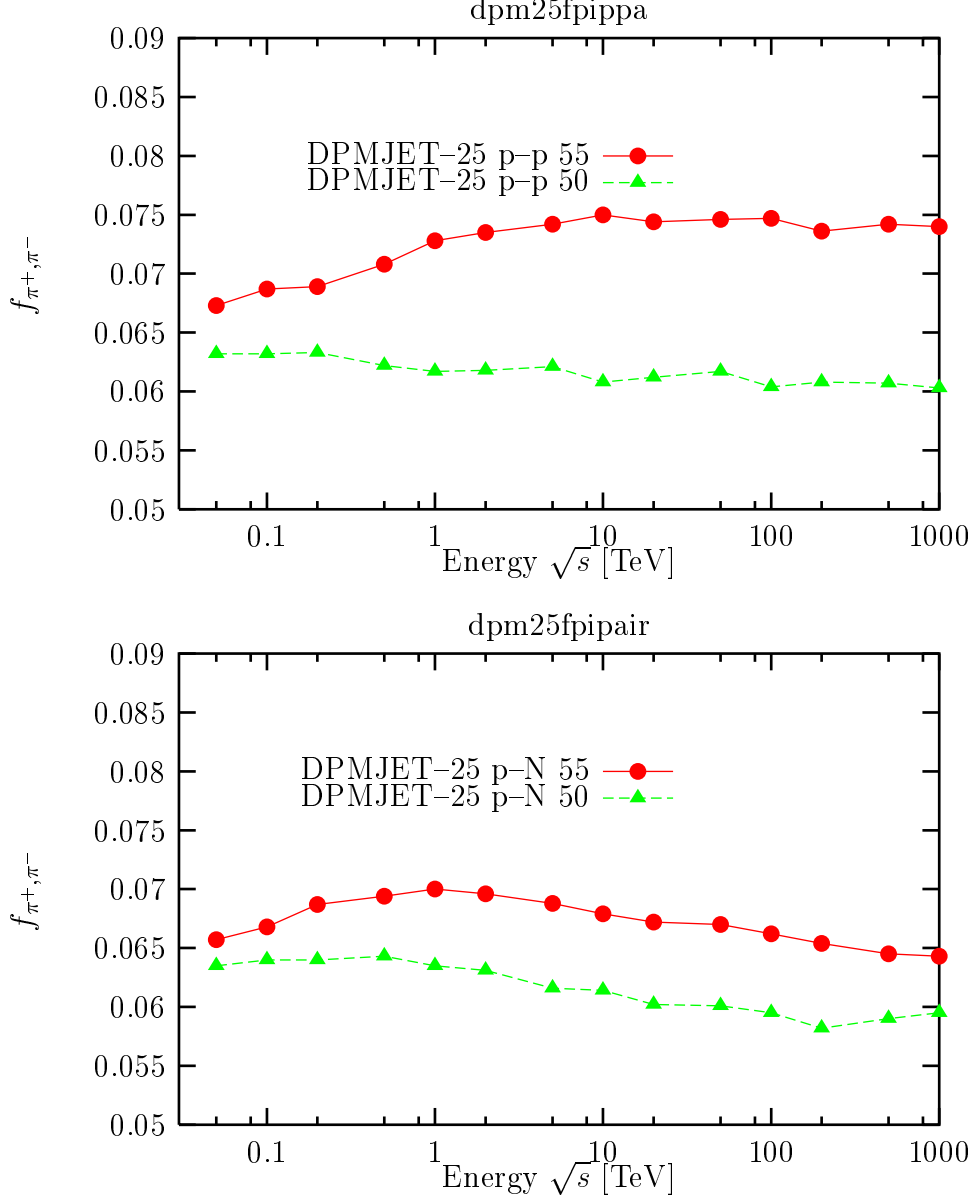


FIG. 29. Spectrum weighted moments for pion production in p-p and p-N collisions as function of the (nucleon-nucleon) cms energy \sqrt{s} .

$$F_i(x_{lab}) = x_{lab} \frac{dN_i}{dx_{lab}} \quad (4.2)$$

We note that the Feynman- x_F distribution at positive x_F in the projectile fragmentation region is a very good approximation to the x_{lab} distribution.

The cosmic ray spectrum-weighted moments in p-A collisions are now defined as moments of the $F(x_{lab})$:

$$f_i^{p-A} = \int_0^1 (x_{lab})^{\gamma-1} F_i^{p-A}(x_{lab}) dx_{lab} \quad (4.3)$$

Here $-\gamma \simeq -1.7$ is the power of the integral cosmic ray energy spectrum and A represents the target nucleus.

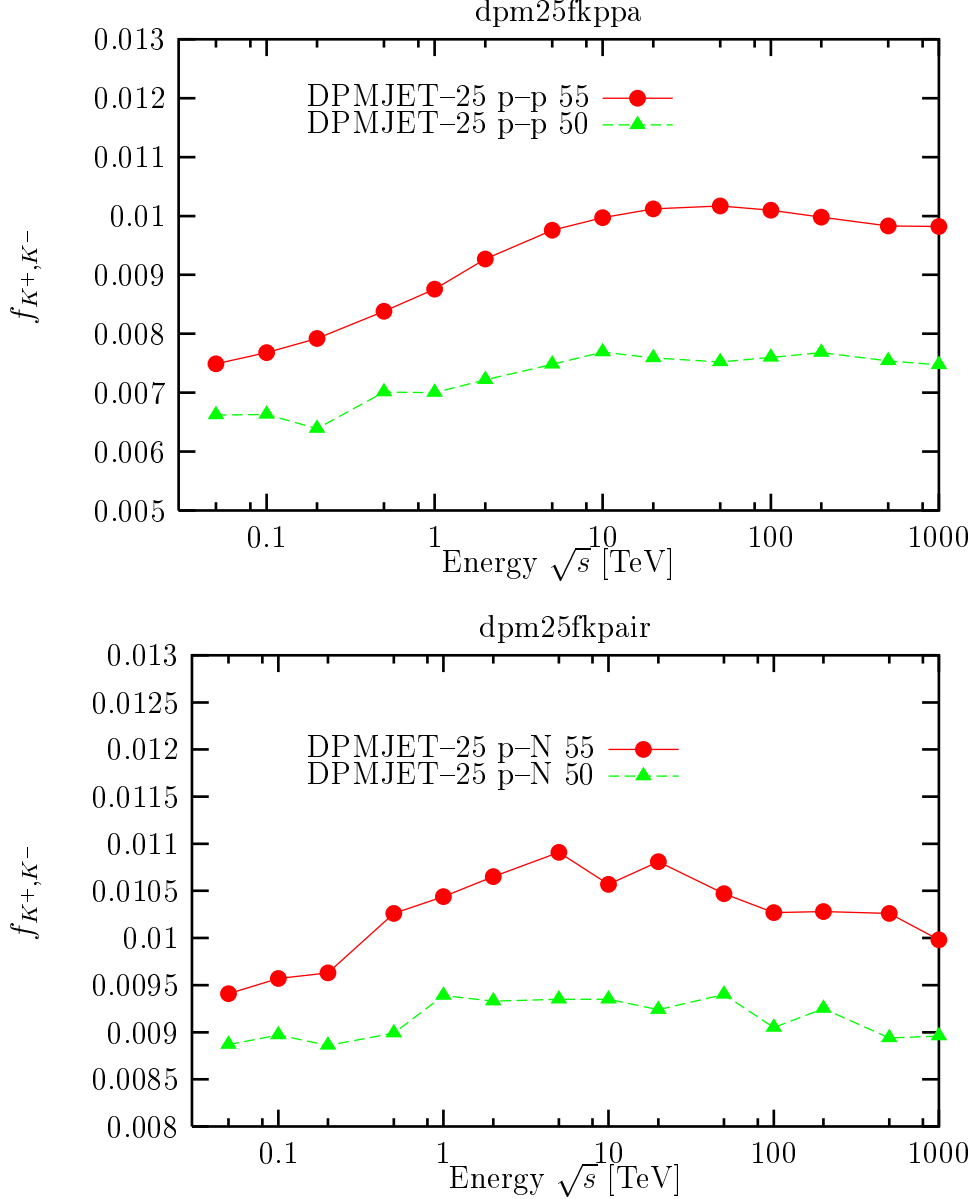


FIG. 30. Spectrum weighted moments for Kaon production in p-p and p-N collisions as function of the (nucleon-nucleon) cms energy \sqrt{s} .

The spectrum-weighted moments for nucleon-air collisions, as discussed in [123], determine the uncorrelated fluxes of energetic particles in the atmosphere.

We also introduce the energy fraction K_i^{p-A} :

$$K_i^{p-A} = \int_0^1 F_i^{p-A}(x_{lab}) dx_{lab} \quad (4.4)$$

As for x_{lab} , the upper limit for K is 1 in h-nucleus collisions.

In Figs.29 we present the spectrum weighted moments summed over pions of both charges in pp and p -N collisions as function of the cms energy \sqrt{s} per nucleon. In Figs.30 the moments are given for charged Kaon production also in pp and p -N collisions.

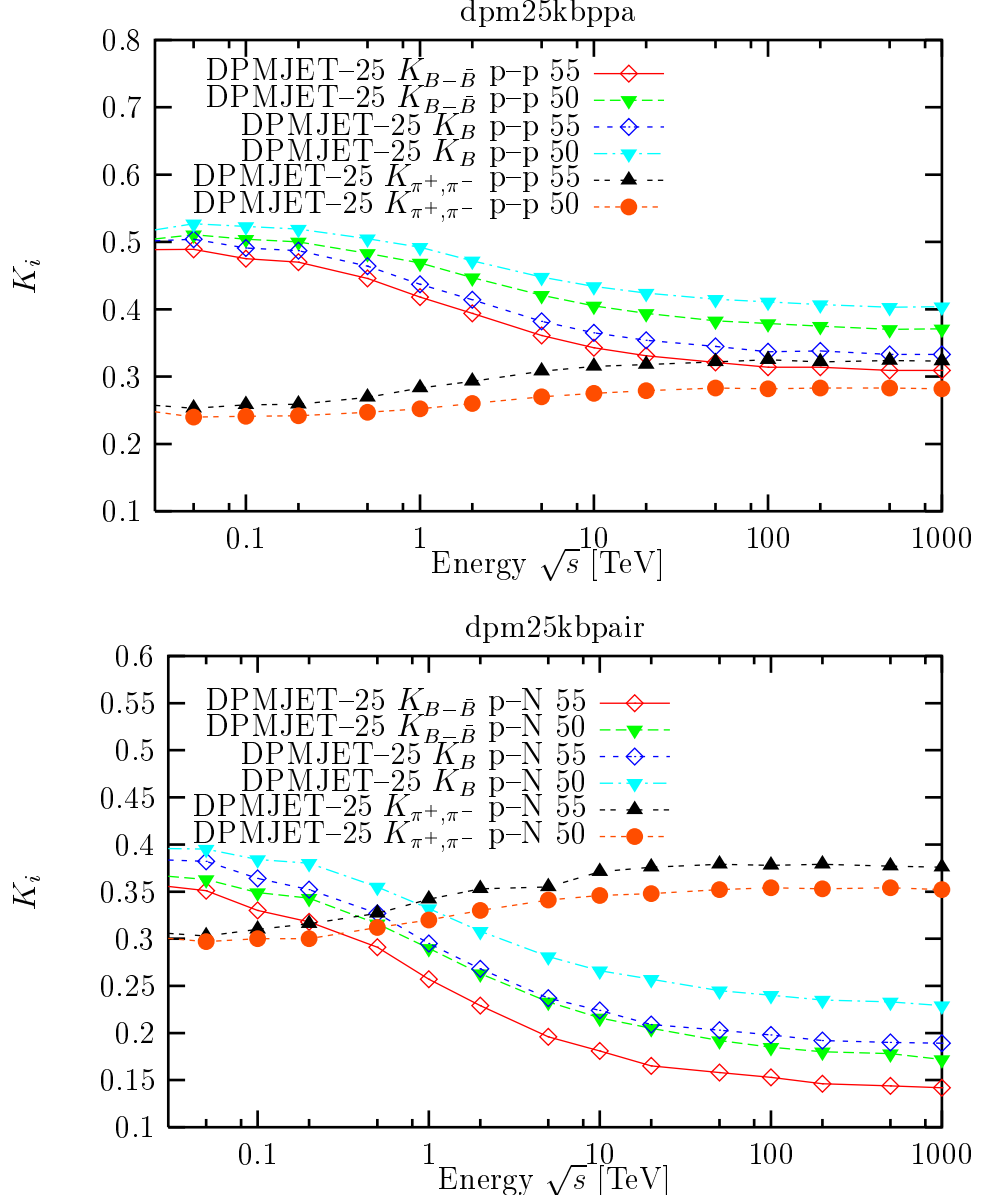


FIG. 31. Laboratory energy fractions for net baryons (baryon minus antibaryon) $B - \bar{B}$, baryons B and charged pion production in p - p and p -N collisions as function of the (nucleon-nucleon) cms energy \sqrt{s} .

In Fig.31 we present again for pp and p -N collisions the energy fractions K for net baryons $B - \bar{B}$ (baryon minus antibaryon), B (baryon) and charged pion production. The energy fraction $K_{B-\bar{B}}$ is always smaller than the energy fraction K_B . The difference between both is the energy fraction going into antibaryons $K_{\bar{B}}$ (not given separately) which is equal to the energy fraction carried by the baryons which are produced in baryon-antibaryon pairs.

We find in DPMJET-II.5 all average values characterizing hadron production: the cross sections (Fig.1), the average transverse momenta (Fig.19) the charged multiplicities (Fig.28), and the moments in Figs. 29, 30 and 31 to change smoothly with energy in most cases just like the logarithm of the energy.

So far, we have not found any experimental data to favour either the versions of DPMJET-II.5 (i or 50) with only GSQBS or (ii or 55) with GSQBS and USQBS. Clearly, the version preferred by theoretical prejudices is (ii or 55). In this version we have a better Feynman scaling of meson distributions and spectrum weighted moments and we have a faster decrease with the collision energy of the energy fractions into secondary baryons.

V. SUMMARY

In the present paper we present new features of the DPMJET-II.5 model and the properties of the model in the Cosmic Ray energy region. The most important of the new features are the new GSQBS and USQBS diagrams, which modify significantly the baryon stopping in the model. Using as well the GSQBS and USQBS options we find significant differences in the high energy behaviour of the new model against former versions of DPMJET.

We report also about comparisons of DPMJET-II.5 with accelerator and collider experiments. We find especially an improved agreement of the Feynman x distributions of leading protons to data and a reasonable agreement to experimental data on leading baryon stopping in nuclear collisions. Many of the published comparisons of former versions of the model to other aspects of experimental data come out quite similar with DPMJET-II.5, we mention especially the properties of the model at low energies [3,29,30] and charm production [39].

There are certainly more tests of the model needed and new features to be incorporated for hadron–nucleus and nucleus–nucleus collisions, for strangeness production and for secondary interactions of the produced particles. DPMJET will continue to evolve, there are already plans for a major new update to DPMJET-III.

ACKNOWLEDGEMENTS

I thank first of all my collaborator Dr. H.-J. Möhring with whom together previous versions of the code up to DTUNUC-I.03 were developed. The author thanks Y. Shmakov for supplying the DIAGEN code prior to publication. Furthermore, the support of CERN , the Department of Theoretical Physics in Lund, INFN, Sezione di Milano , INFN,LNF Frascati, LAPP Annecy, The University Santiago de Compostela and INFN, Lab. Naz. del Gran Sasso and Siegen University where parts of the program were developed is acknowledged. The code in the version described here was finalized at Siegen. The author acknowledges the fruitful collaborations with P.Aurenche, G.Battistoni, F.Bopp, M.Braun, A. Capella, R.Engel, A.Ferrari, C.Forti, K.Hänßgen, K.Hahn, I.Kawrakov, C.Merino, N.Mokhov, H.J.Möhring, C.Pajares, D.Pertermann, S.Ritter, S.Roesler, P.Sala and J.Tran Thanh Van on the Dual Parton Model in general and he thanks G.Battistoni, F.Bopp, R.Engel and S.Roesler for useful comments on this paper.

[1] J. Ranft: DPMJET version II.5, Sampling of hadron–hadron, hadron–nucleus and nucleus–nucleus interactions at accelerator and Cosmic Ray energies according to the two–component Dual Parton Model, code manual, Siegen preprint, , 1999

[2] J. Ranft: Phys. Rev. D 51 (1995) 64

[3] J. Ranft: DPMJET-II, a Dual Parton Model event generator for hadron–hadron, hadron–nucleus and nucleus–nucleus collisions, Proceedings of the second SARE workshop at CERN, 1995,ed. by G.R.Stevenson, CERN/TIS-RP/977-05, p. 144., 1997

[4] J. Ranft: DPMJET-II, sampling of hadron–hadron, hadron–nucleus and nucleus–nucleus interactions according to the dual parton model, , unpublished code write–up , CERN, 1995

[5] J. Ranft: DPMJET versions II.3 and II.4 Sampling of hadron–hadron, hadron–nucleus and nucleus–nucleus interactions at Cosmic Ray energies according to the Dual Parton Model, description of the model and code manual, Gran Sasso INFN/AE-97/45, 1997

[6] M. Glück, E. Reya and A. Vogt: Z. Phys. C67 (1995) 433

[7] M. Glück, E. Reya and A. Vogt: Eur. Phys. J. C5 (1998) 461

[8] G. Battistoni, M. Carboni, C. Forti and J. Ranft: Release of a new version (V.07–1) of he HEMAS–DPM Monte Carlo. Description and users manual., Gran Sasso preprint INFN/AE-99/07, 1999

[9] G. F. Chew and C. Rosenzweig: Nucl. Phys. B104 (1976) 290

[10] H.-M. Chan, J. E. Paton and S. T. Tsou: Nucl. Phys. B86 (1975) 479

[11] A. Capella, U. Sukhatme, C. I. Tan and J. Trần Thanh Vân: Phys. Lett. B81 (1979) 69

[12] A. Capella, U. Sukhatme, Chung I Tan and J. Tran Thanh Van: Phys. Rep. 236 (1994) 225

[13] R. Engel: Hadronic Interactions of Photons at High Energies, Thesis, Siegen University, available from web–site <http://lepton.bartol.udel.edu/~eng/phojet.html> , unpublished, 1997

[14] A. Capella, J. Tran Thanh Van and J. Kwiecinski: Phys. Rev. Lett. 58 (1987) 2015

[15] P. Aurenche, F. W. Bopp, A. Capella, J. Kwiecinski, M. Maire, J. Ranft and J. Tran Thanh Van: Phys. Rev. D45 (1992) 92

[16] F. W. Bopp, A. Capella, J. Ranft and J. Tran Thanh Van: Z. Phys. C51 (1991) 99

[17] F. W. Bopp, D. Pertermann and J. Ranft: Z. Phys. C54 (1992) 683

[18] R. Engel, F. W. Bopp, D. Pertermann and J. Ranft: Phys. Rev. D46 (1992) 5192

[19] S. Roesler, R. Engel and J. Ranft: Z. Phys. C59 (1993) 481

[20] F. W. Bopp, D. Pertermann, R. Engel and J. Ranft,: Phys. Rev. D 49 (1994) 3236

[21] B. L. Combridge, J. Kripfganz and J. Ranft: Phys. Lett. 70B (1977) 234

[22] J. Ranft and S. Ritter: Z. Phys. C 20 (1983) 347

[23] J. Ranft and S. Ritter: Z. Phys. C 27 (1985) 569

[24] H.-J. Möhring, J. Ranft and S. Ritter: Z. Phys. C 27 (1985) 419

[25] J. Ranft : Phys. Lett. 188B (1987) 379

[26] J. Ranft : Z. Phys. C 43 (1989) 439

[27] L. Landau and I. Pomeranchuk: Dokl. Akad. Nauk SSR 92 (1953) 535, 734

[28] L. Stodolski: Proc. Vth Intern. Colloquium on Multiparticle Reactions Oxford (1975) 577

[29] A. Ferrari, J. Ranft, S. Roesler and P. R. Sala: Z. Phys. C70 (1996) 413

[30] A. Ferrari, J. Ranft, S. Roesler and P. R. Sala: Z. Phys. C71 (1996) 75

[31] J. Ranft: Phys. Rev. D37 (1988) 1842

[32] H.-J. Möhring and J. Ranft: Z. Phys. C52 (1991) 643

[33] I.Kawrakow, H.-J.Möhring and J.Ranft: Nucl. Phys. A544 (1992) 471

[34] I.Kawrakow, H.-J.Möhring and J.Ranft: Z. Phys. C56 (1992) 115

[35] H.-J. Möhring, J. Ranft, A. Capella and J. Tran Thanh Van: Phys. Rev. D47 (1993) 4146

[36] S. Roesler, R. Engel and J. Ranft: Z. Phys. C59 (1993) 481

[37] J. Ranft, A. Capella and J. Tran Thanh Van: Phys. Lett. B320 (1994) 346

[38] A. Capella and J. Tran Thanh Van and J. Ranft: Nucl. Phys. A 566 (1994) 511c

[39] G. Battistoni, C. Bloise, C. Forti, M. Greco, J. Ranft and A. Tanzini: Astroparticle Physics 4 (1996) 351

[40] G. Battistoni, C. Forti and J. Ranft: Astroparticle Phys. 3 (1995) 157

[41] G. Battistoni, C. Forti, J. Ranft and S. Roesler: Astropart. Phys. 7 (1997) 49

[42] G. Battistoni, P. Lipari, J. Ranft and E. Scapparone: Simulation of nuclear effects in quasielastic and resonant neutrino interactions, Gran Sasso INFN–AE-03–98, hep-ph/9801426, 1998

[43] R. V. Barrett and D. F. Jackson: *Nuclear sizes and structure*, Clarendon Press, Oxford 1977

[44] S. Roesler, R. Engel and J. Ranft: Phys.Rev. D57 (1998) 2889

[45] S. Roesler: personal communication, 1999

[46] S. Ritter: Comput. Phys. Commun. 31 (1984) 393

[47] J. Ranft and S. Ritter: Acta Phys. Pol. B 11 (1980) 259

[48] NA35 Collaboration, T. Alber et al. : Z. Phys. C 64 (1994) 195

[49] NA35 Collaboration, T. Alber et al. : Eur. Z. Phys. C2 (1998) 643

[50] A. Capella and B. Kopeliovich: Phys. Lett. B381 (1996) 325

[51] A. Capella, E. G. Ferreiro and C. A. Salgado: Phys. Lett. B459 (1999) 27

[52] A. Capella and C. A. Salgado: hep-ph/9903414, preprint LPT Orsay 99-20 (1999)

[53] J. A. Casado: hep-ph/9810357v3, Manchester preprint MC-TH-98-17 (1999)

[54] A. Donnachie and P. V. Landshoff: Phys. Lett. B296 (1993) 227

[55] G. Arnison et al.: Phys. Lett. B128 (1983) 336

[56] UA4 Collab.: M. Bozzo et al.: Phys. Lett. B147 (1984) 385

[57] N. A. Amos et al.: Nucl. Phys. B262 (1985) 689

[58] UA4 Collab.: D. Bernard et al.: Phys. Lett. B198 (1987) 583

[59] UA5 Collab.: G. J. Alner et al.: Z. Phys. C32 (1986) 153

[60] E710 Collab.: N. A. Amos et al.: Phys. Lett. B243 (1990) 158

[61] CDF Collab.: F. Abe et al.: FERMILAB-PUB-93/234-E, 1993

[62] CDF Collab.: F. Abe et al.: Phys. Rev. D50 (1994) 5518

[63] CDF Collab.: F. Abe et al.: Phys. Rev. D50 (1994) 5550

[64] CHLM Collab.: M. G. Albrow et al.: Nucl. Phys. B108 (1976) 1

[65] CHLM Collab.: J. C. M. Armitage et al.: Nucl. Phys. B194 (1982) 365

[66] E710 Collab.: N. A. Amos et al.: Phys. Lett. B301 (1993) 313

[67] CDF Collab.: F. Abe et al.: Phys. Rev. D50 (1994) 5535

[68] UA4 Collab.: D. Bernard et al.: Phys. Lett. B186 (1987) 227

[69] R. Engel: Z. Phys. C66 (1995) 203

[70] E. Gotsman, E. M. Levin and U. Maor: Phys. Rev. D49 (1994) 4321

[71] K. Goulianos: Phys. Lett. B358 (1995) 379

[72] H.H.Mielke, M.Föller, J.Engler and J.Knapp : J.Phys. G 20 (1994) 637

[73] Akeno Collab.: M. Honda et al.: Phys. Rev. Lett. 70 (1993) 525

[74] Fly's Eye Collab.: R. M. Baltrusaitis et al.: Phys. Rev. Lett. 52 (1984) 1380

[75] M. M. Block, F. Halzen and T. Stanev: Predicting proton-air cross sections at $\sqrt{s} \approx 30$ TeV using accelerator and Cosmic Ray data, hep-ph/9908222, 1999

[76] J. Ranft and S. Roesler: Z. Phys. C62 (1994) 329

[77] S.Yu.Shmakov, V.V.Uzhinskii and A.M.Zadoroshny: Comp.Phys.Comm. 54 (1989) 125

[78] R.Castaldi and G.Sanguinetti : Ann.Rev.Nucl.Part.Sci. 35 (1985) 351

[79] Particle Data Group: Phys. Rev. D45 (1992) 1

[80] G. C. Rossi and G. Veneziano: Nucl. Phys. B123 (1977) 507

[81] U. Sukhatme, K. Lassila and R. Orava: Phys. Rev. D25 (1982) 2075

[82] B. Z. Kopeliovich and B. G. Zakharov: Z. Phys. C43 (1989) 241

[83] T. Sjöstrand: Comp. Phys. Comm. 82 (1994) 74

[84] B. Andersson, G. Gustafson and T. Sjöstrand: Physica Scripta 32 (1985) 574

[85] A. Capella: Standard sources of particle production in heavy ion collisions, hep-ph/9910219, 1999

[86] S. E. Vance and M. Gyulassy: Anti-Hyperon enhancement through baryon junction loops, Cu-YP-929, nucl-th/9901009, unpublished, 1999

[87] J. Rafelski and B. Müller: Phys. Rev. Lett. 48 (1982) 1066

[88] P. Koch, J. Rafelski and B. Müller: Phys. Rep. 142 (1986) 167

[89] J. Ranft, A. Capella and J. Trần Thanh Vân: Phys. Lett. B320 (1994) 346

[90] H.-J. Möhring, J. Ranft, A. Capella and J. Trần Thanh Vân: Phys. Rev. D47 (1993) 4146

[91] A. Capella : Phys. Lett. B384 (1995) 175

[92] A. Capella, A. Kaidalov, A. Kouider Akil, C. Merino, J.Tran Thanh Van: Z.Phys. C 70 (1996) 507

[93] C. Merino and C. Pajares and J. Ranft: Phys. Lett. B 276 (1992) 168

[94] H.-J. Möhring, J. Ranft, C. Merino and C. Pajares: Phys. Rev. D47 (1993) 4142

[95] N. Armesto, M. A. Braun, E. G. Ferreiro and C. Pajares: Phys. Rev. Lett. 77 (1996) 3736

[96] M. A. Braun, C. Pajares and J. Ranft: , hep-ph/9707363, Santiago preprint US-FT/24-97, , 1997

[97] N. Armesto and A. Capella: Phys. Lett. B393 (1997) 431

[98] N. Armesto, A. Capella and E. G. Ferreiro: Phys. Rev. C59 (1999) 395

[99] K. Hänssgen and J. Ranft: Comp. Phys. Commun. 39 (1986) 37

[100] K. Hänssgen and J. Ranft: Nucl. Sci. Eng. 88 (1984) 537

[101] M.Gazdzicki and O.Hansen : Nucl. Phys. A 528 (1991) 754

[102] LEBC-EHS Collab.: M. Aguilar-Benitez et al.: Z. Phys. C50 (1991) 405

- [103] NA22 Collab.: M. Adamus et al.: Z. Phys. C39 (1988) 311
- [104] A. E. Brenner et al.: Phys. Rev. D26 (1982) 1497
- [105] M. Basile and Others: Lett. Nuovo Cim. 41 (1984) 298
- [106] R. S. Fletcher, T. K. Gaisser, P. Lipari and T. Stanev: Phys. Rev. D50 (1994) 5710
- [107] N. Kalmykov and et al.: Physics of Atomic Nuclei 58 (1995) 1728
- [108] ZEUS Coll.: A. Garfagnini and et al: Proc. Sixth Int. Workshop on Deep Inelastic Scattering and QCD, Brussels (1998)
- [109] H1 and ZEUS Coll.: W. Schmidke: Proc. XXIXth Int. Conf. on High Energy Physics, Vancouver, Canada (1998)
- [110] R. Engel, T. K. Gaisser and T. Stanev: Extensive air showers and hadronic interaction models, Talk at the ISMD99 Symposium Providence R.I. , unpublished, 1999
- [111] R. Engel: Nucl. Phys. (Proc. Suppl.) 75A (1999) 62
- [112] UA1 Collab.: C. Albajar et al.: Nucl. Phys. B335 (1990) 261
- [113] G. Bocquet et al.: Phys. Lett. B366 (1996) 434
- [114] T. Alexopolous and et al: Phys. Rev. D 48 (1993) 984
- [115] NA35 Collaboration, J.Bartke et al. : Z. Phys. C 48 (1990) 191
- [116] C. De Marzo et al.: Phys. Rev. D26 (1982) 1019
- [117] D. H. Brick and et al: Phys. Rev. D39 (1989) 2484
- [118] NA35: J. Bächler and et al: Z. Phys. C51 (1991) 157
- [119] NA-35: P. Seyboth: J. Phys. G, Nucl. Part. Phys. 23 (1997) 1787
- [120] ALICE Collaboration: ALICE technical proposal, CERN report CERN/LHCC/95-71, 1995
- [121] NA-44: I. Bearden and et al: Strange meson enhancement in Pb–Pb collisions, nucl-ex/9907013, 1999
- [122] NA36: E. Judd and et al: Nucl. Phys. A590 (1995) 291
- [123] T. K. Gaisser: *Cosmic Rays and Particle Physics*, Cambridge University Press, 1990